Journal of Molecular Structure 1329 (2025) 141452

Contents lists available at ScienceDirect

Journal of Molecular Structure

journal homepage: www.elsevier.com/locate/molstr

Crystalline phases of ZnS: A systematic investigation and its effect on photodegradation of dye pollutant

Rohini A. Khaparde [a,b,*], Smita A. Acharya [a], Priya Tumram [c], Shahin Sayyed [d]

[a] Department of Physics, RTM Nagpur University, Nagpur 440033 M.S., India
[b] GH.Raisoni college of Engineering, CRPF Gate, No.3, Hingna Road, Digdoh Hills, Nagpur 440016, M.S., India
[c] Department of Physics, Amolakchand Mahavidyalaya, Yavatmal 445001 M.S., India
[d] Department of Physics, Shivaji Science College, Congress Nagar, Dhantoli, Nagpur 440012, India

ARTICLE INFO

Keywords:
Ethanolamine
ZnS
Nanoparticles
Photocatalysts
Malachite green
Photodegradation

ABSTRACT

In the present investigation, surface capping agent induced structural phase transition of doped-ZnS and its influence on photodegradation behaviors of organic dye are systematically explored. Role of Ethanolamine (EA) as surface capping agent during synthesis of doped ZnS are revealed. Interestingly, high temperature Wurtzite phase of ZnS, which typically occurring at 1020 °C; is obtained at a significantly lower temperature of 120 °C via simple co-precipitation method in presence of EA. The results are repeated in presence of Mn, Cu, Co, and Cd as dopant in ZnS for the compositions $Zn_{0.94}D_{0.06}S$ (where D is dopant). The EA-mediated phase transformation (zinc blende to wurtzite) of all doped-ZnS systems are confirmed from the X-ray diffraction study. Scanning electron microscopy (SEM) and transmission electron microscopy (TEM) images display nanoscale dimensions (at the range 10–40 nm) of as-synthesized ZnS samples. Phase transition effect on local-level structural changes is revealed by Raman Spectroscopy. UV–VIS spectra exhibit notable lower side wavelength shift (blue shift) in the ZnS system. Additionally, photoluminescence (PL) spectra also replicate surface capping agent effect on phase transition in doped-ZnS system. The influence of ZnS phases (zinc blende and wurtzite) on the photodegradation of dye pollutants are comprehensively studied using malachite green. The influence of various parameters such as: (1) content of the ZnS system, (2) effect of irradiation time, (3) pH and scavengers are investigated by analyzing the rate of de-coloration of dye using UV–VIS absorption. The degradation kinematic reveals that Wurtzite ZnS is more efficient than Cubic-phase. Hydrogen peroxide at 500 mg/L acts as electron scavenger, thus enhances degradation efficiency. The study depicts that wurtzite phase of nanoparticles of doped ZnS is more dominant in photodegradation and prospective system for water purifications of organic dye polluted water.

1. Introduction

II-VI semiconductor nanoparticles encompass unique electronic, optical, and physical properties, giving them a stand in research and technologies. These properties strongly hang on the structure, morphology, and particle size [1–4]. This group of semiconductors shows a drastic change in the properties when the radius of the particle is comparable to Bohr's excitonic radius [5–7]. Such small particle size and large band gap semiconductors lead to a great number of surface states and defects in the crystal. This provides us with novel opportunities for optical studies and advances its applications [8,9], New energy levels develops in between valence band (V.B.) and Conduction band (C.B.) of host crystal lattice on doping it with transition metals such as Mn, Ni, Fe, Ag, etc. This results in modification of optical properties and shifts light absorption from UV towards VLA, along with controlled particle size and shortened lifetime from ms to ns [10–14].

Among the semiconductors discovered, ZnS is one of the most important wide band gap semiconductors ever discovered and has a great attraction in the field of research. Its properties are widely tunable by the doping effect. Doped ZnS with transition metal dopant elements can tune the structure and physical properties of the host lattice [15–17]. These systems exhibit outstanding applicability in versatile fields such as photocatalysis, solar cells, sensors, imaging, electro-optic devices, flat panels, H_2 evolution, etc. [18–21] Photocatalysis is a technique in which ZnS acts as photocatalysts, and degradation of dye pollutant of water takes palace on the surface of ZnS via redox reaction

* Corresponding author.
E-mail address: raask5341@gmail.com (R.A. Khaparde).

https://doi.org/10.1016/j.molstruc.2025.141452
Received 30 January 2024; Received in revised form 11 January 2025; Accepted 13 January 2025
Available online 14 January 2025

[22]. Dyes are used in most industries such as textile, photographic paper, printer industries, and many more Azo organic dyes and their intermediates are highly toxic, carcinogenic, non-biodegradable tumors causing to several parts of humans, and hazardous to the ecosystem [23, 24]. Malachite Green (MG), a cationic triphenylmethane dye, finds wide application across various industries including textiles (for dyeing silk and wood), leather, paper, and pharmaceuticals. However, MG poses significant risks to both human health and the environment. Its adverse effects extend to the immune and reproductive systems of living organisms, and it is known to possess genotoxic and carcinogenic properties [25,26]. Even in its reduced form, known as leucomalachite green, it presents potential hazards to human health. Due to its extensive use, MG contamination in waterways via industrial waste is pervasive, constituting a substantial proportion of water pollution. Hence, the imperative to convert toxic and non-biodegradable organic contaminants into non-toxic forms directly at industrial discharge points is paramount. Among the array of water purification methods developed to date, semiconductor photocatalytic degradation stands out as a pivotal technique. Its ability to achieve the complete mineralization of toxic organic dyes without generating any residual forms underscores its significance [27–29]. Furthermore, this technique leads to the degradation of dye with "high efficiency, strong oxidizing power, non-toxicity, high photochemical and biological stability, corrosive resistance and low cost", which make it superior to other water purification techniques namely coagulation, flocculation, absorption, and membrane technologies merely make the wastes concentrated or transfer the contamination from one phase to another and thus produce another kind of pollutant which requires further treatment" [30,31].

ZnS is a trimorphic crystal having three polymorphs it i.e. Zinc blende, rhombohedral, and wurtzite. Sphalerite (cubic phase) and wurtzite (hexagonal phase) are the two main polymorphic forms of it while the Rhombohedral structure is an intermediate phase between them and forms at 600 °C [32]. At ambient conditions, the sphalerite structure is the most stable form, and in bulk, it possesses a band gap of 3.66 eV It is the phase, that has a "face-centered cubic structure having dual structural motif, in which Zn occupies (0,0,0) and S occupiers (¼,¼,¼,) sites." While the high-temperature wurtzite phase is a thermodynamically metastable state and exhibits a band gap of 3.77 eV at room temperature. "This structure is stable at 1020 °C and melts at 1650 °C. In wurtzite structure Zn occupies (1/3, 2/3, 0) and S occupiers (1/3, 2/3, 0.3748) sites. In both structures, Zn and S are tetrahedrally bonded with the only difference in the stacking sequence of atomic layers. In cubic Zn and S stacked in ABCABC….. pattern, while that in hexagonal structures in ABABAB….. ." [33–35] These differences in their crystalline structure and size can lead to considerable changes in the effective masses of electrons, holes, and energy gaps [10,35,36]. So, it is very important to investigate the effect of both crystalline structures of ZnS on the photodegradation process. To date, studies on photodegradation using ZnS nanoparticles (NPs) have focused on individual phases without offering a comparative analysis. Motivated by this gap, our previous research systematically investigated photodegradation using pure and doped ZnS samples with a cubic structure [10]. Building on this foundation, we have endeavored to systematically compare the photodegradation efficiency of dyes using ZnS samples possessing both cubic and wurtzite structures, with particle size control implemented. Additionally, we successfully incorporated transition metal ions through doping in both structures and conducted a comparative analysis of their photodegradation capabilities.

2. Experimental

2.1. Materials

All chemical reagents i.e. Zinc acetated [(Zn $(CH_3COO)_2$. $2H_2O$) 98 % and 99.99 %], Sodium sulfide flakes ($Na_2S.xH_2O$), Cadmium acetated [($C_4H_6CdO_4$) 98 %], Copper acetated, Cobalt acetate and Manganous acetated [($Mn(CH_3COO)_2{\cdot}4H_2O$) 99 %] were used as it is without any purification and procured from Merck, Sigma-Aldrich, and Qualigens. Aqueous solutions were prepared by using double distilled water and Ethanolamine throughout its preparation. The Malachite Green stock solution (concentration of 0.5 mgL^{-1}) was prepared by dissolving Malachite Green oxalate powder (CAS.No.2437–29–8) in double distilled water.

2.2. Synthesis of ZnS nanoparticles

The detailed synthesis procedure for pure and doped ZnS samples with a cubic phase is provided in our previous publication [10]. For Wurtzite ZnS, 100 ml ethanolamine was taken in a beaker, and Zinc acetate (0.1 mole) was added in it. The mixed solution was kept for constant stirring on a hot plate with a magnetic stirrer for 30 min at 60 ^{0}C. 0.1 ml of Na_2S was then added into it resulting in a white solution. To get a homogeneous mixing of all the precursors, the white solution is again stirred for 30 min at 60 ^{0}C. The resulting solution was then transferred into a flask with reflexure and condenser and heated for 24 hr. at 120^{0}C. The washing of the obtained solution was done with water by centrifuging it for 15 min at 6000 rpm. and the precipitate was dried in a hot air vacuum oven at 60^{0}C. Doped ZnS samples are prepared by the same method as done above and are repeated only replacing a few percentages of Zinc Acetated by dopant using the formula $Zn_{(1-x)}M_{(x)}S$, where M was Mn, Cu, Co, and Cd. The same method as done above is repeated only replacing a few percentages of Zinc Acetated by dopant using the above formula.

2.3. Characterizations

To check the structure and phase purity of the sample X-ray powder diffraction (XRD) study is done. PAN analytical X Pert Pro X-ray diffractometer equipped with the copper target (λ_1, $CuK\alpha_1$=1.5405 A^0) is used for it. The data were collected with a step size of 0.016711^0 and a step time of 5 .08s. By using software namely "Full Pro Suit", the Rietveld refinement of the XRD pattern was done. Scanning electron microscopy (SEM) images were obtained on JSM-7600F, equipped with an energy-dispersive X-ray spectroscopy. Transmission electron microscopy (TEM) images were obtained on a Philips CM200 transmission electron microscope with an operating voltage of 20–200 kV and a resolution 2.4 A^0. Absorption spectra were obtained on a Perkin Elmer Lambda 35 Serial No 502,512,621,910 UV–vis spectrometer. Raman spectra of samples were obtained from Micro Raman System from Jobin Yvon Horibra LABRAM-HR visible (400–1100 nm) having Raman shift range of 50 cm^{-1} to 4000 cm^{-1} with a resolution of 1 cm^{-1}. Photoluminescence spectra of samples were recorded at room temperature using spectrophotometer RF5301 with excitation wavelengths 265 nm and 260 nm.

2.4. Photocatalytic degradation of malachite green

The photocatalytic dye degradation ability of ZnS (Cubic and Wurtzite) was studied for Malachite Green (MG) dye under UV–Vis irradiation degradation. The absorption spectra of MG samples at λ_{max} of 617 nm were obtained on a UV–vis spectrometer. The changes in the value of absorbance of the samples at λ_{max} of dyes: (a) with the variation in the concentration of the samples. (b) After irradiation in a certain interval of time showed the rate of decolorization and therefore, Photodegradation efficiency of the dyes. (c) The degradation efficiency was calculated as:

$$\% D.E = \left(\frac{A_0 - A_t}{A_0}\right) \times 100 \quad (1)$$

where, A_o and A_t are the initial absorbance and final absorbance of dye before and after photoirradiation (time *t)*, respectively and *t* is

irradiation time of sample.

(d) The photocatalytic reaction rate are calculated by using Pseudo first-order kinetic analysis using the equation:

$$\ln\frac{C}{C_o} = -kKt = k_{obs}t \quad (2)$$

In which k_{obs} is observed first-order rate constant of the photo-degradation reaction which can be calculated using the plot of $\ln(C/C_o)$ vs *time*.

3. Results and discussion

3.1. X-ray diffraction

The XRD patterns of both pure and doped ZnS samples in the wurtzite structure are illustrated in Fig. 1. The XRD patterns of the cubic phase of pure ZnS and doped ZnS can be found in our earlier report [10]. These patterns reveal broadened diffraction peaks compared to those of bulk ZnS crystals, confirming the finite size of the crystallites, except for the case of Cu-doped wurtzite ZnS (Fig. 1**e**), which exhibits sharp peaks. In our current approach utilizing EA as a solvent, the XRD pattern displays peaks at 28.87°, 48.04°, and 56.74° characteristic of the cubic zinc blende phase. However, alongside these existing peaks, new additional peaks appear at 2θ = 27.49°, 31.09°, 40.28°, and 52.61°, overlapping with them. All these peaks correspond to the planes (100), (002), (101), (102), (110), (103), and (112) of the wurtzite phase of ZnS (JCPDS card no 751,534). The good match between all diffraction peaks of the sample and those of the wurtzite phase of ZnS crystal indicates the formation of the wurtzite phase in the ZnS sample when EA is used as the solvent. Interestingly, the wurtzite structure remains unchanged even in the presence of dopants, suggesting solid solution formation even with EA as the solvent, while maintaining a finite crystalline size.

The structural phase refinement of pure and doped Wurtzite ZnS is done by Rietveld refinement of the XRD (Fig. 2). The samples were confirmed with a space group of P 6_3 mc. All the samples exhibit goodness of fit in the range 1–2. This indicates acceptable fits by using Rietveld refinement. The parameters found from Rietveld refinement have been tabulated in Table 1. The Rietveld refined data fitted with the space group of Wurtzite ZnS shows a very small percentage of Cubic phases but the dominancy of the Wurtzite phase can be clearly seen. On doping the host crystal (ZnS) with isovalent dopants (Mn, and Cd) having a little higher ionic radius than the host, led to a decrease in the percentage of Cubic structure. In the case of Co and Cu which have a slightly lower ionic radius than the host, led to an increase in the percentage of Cubic structure. Thus, enhancement in the wurtzite structure by an isovalent dopant with a slightly higher ionic radius can also be understood.

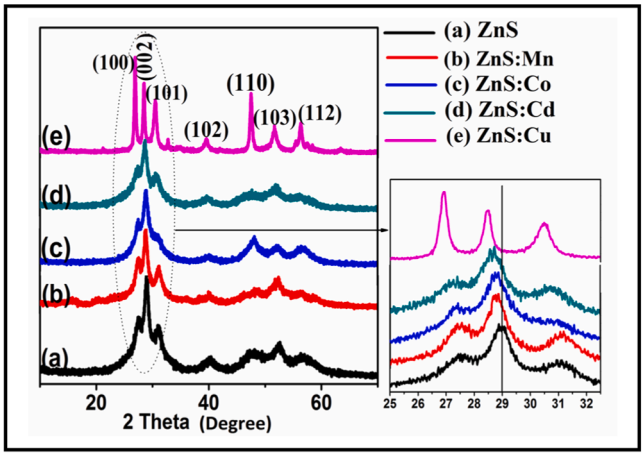

Fig. 1. XRD pattern of as synthesized ZnS having wurtzite Phase: (a)ZnS, (b) Mn, (c)Co, (d)Cd, (e)Cu doped ZnS.

To analyze the dopant effect in ZnS having a Wurtzite phase more comprehensively, the VESTA program generates a three-dimensional view of the crystal structure of ZnS using XRD data. Microscopic structural information like bond angle, bond length difference, and tilting angle are extracted out from this modern fitting. The pictorial representation of the crystal structure of doped and undoped ZnS having Wurtzite phase is depicted in Fig. 3. In ZnS, "Zn occupies the central position with four equally spaced S atoms forming a tetrahedral geometry." As the Rietveld refinement of the XRD pattern confirmed the presence of a very small percentage of cubic phase in the Wurtzite structure; a 3D view of the crystal structure also exhibits the same. In cubic structure, all bond lengths are equal in length and have a constant bond angle and bridging angle of 109.47. In the case of Wurtzite structure bond length and bond angle are quite different in different directions. Letters '1, 2, 3, and 4′ are used to designate bond length along four different directions of tetrahedral ZnS_4. Bond length '2′ is quite large compared to the other three bond lengths. The bond angle '1′ and '2′ are found same and the bond angles '3′ and '4′ are the same. Both doped and undoped wurtzite ZnS exhibit similar structures. The only difference is that partially Zn is replaced by a dopant. The obtained data of bond angle and length from the VESTA program fitting is tabulated in Table 2.

Variation trends of parameters like bond length and bond angle as a function of dopants are analyzed by plotting the parameters against the ionic size of dopants. Fig. 4. depicts the variation in bond length with the increase in ionic radii of dopants. As mixed phases are formed in the presence of EA, variation in the bond length of Cubic as well as Wurtzite structure can be observed. The bond length of the Cubic phase and bond length 2 of the Wurtzite phase show an increasing trend with the rise in ionic size of dopants while the bond length of bonds 1, 3, and 4 show a reverse pattern. Fig. 5. depicts the relation between the bond angles of the wurtzite phase of doped ZnS and ionic radii of dopants. Bond angles 1 and 2 show a decreasing trend while Bond angles 3 and 4 show an increasing trend with the increases in ionic radii of the dopants.

3.2. Microstructure by SEM and TEM

To extract microstructural information, an SEM and TEM study of the ZnS sample was performed. SEM image of as-synthesized (A) Cubic (pure and doped) and (B) Wurtzite (pure and doped) ZnS NPs is shown in Fig. 6. SEM images display spherical morphology and a relatively narrow size distribution for all the particles. The particle size ranges from 10 nm to 15 nm in the case of pure cubic ZnS while it is approximately 20 nm to 25 nm for doped cubic ZnS. A slight increase in the particle size can be noticed with the doping in the host [Fig. 6**(A)**]. In the case of Wurtzite (both pure and doped) ZnS the particle size ranges from 25 nm to 35 nm [Fig. 6**(B)**].

TEM images of as-synthesized ZnS samples again confirmed a very fine particle size of about 20 nm with spherical morphology for all the samples. [Fig. 7] The SAED image in insert of Fig. 7**(A)** shows continuous lattice fringes, which is in good agreement with the lattice spacing in the (111), (220) and (311) planes of cubic ZnS. While in Fig. 7**(B)** shows continuous lattice fringes, which is in good agreement with the lattice spacing in the (100), (002), (101), (102), (110), (103), and (112) planes of Wurtzite ZnS. The SAED ring patterns of all the samples are found consistent with a polycrystalline nature.

3.3. Raman spectroscopy studies

To study the atomic scale restructuring in cubic and wurtzite phase of ZnS are studied by using Raman spectroscopy tools. The experimental data is fitted by Gaussian to extract various vibration modes. Fig. 8 exhibits experimental and fitted Raman spectra at room temperature. The wave numbers of the identified phonon mode for both spectrums are

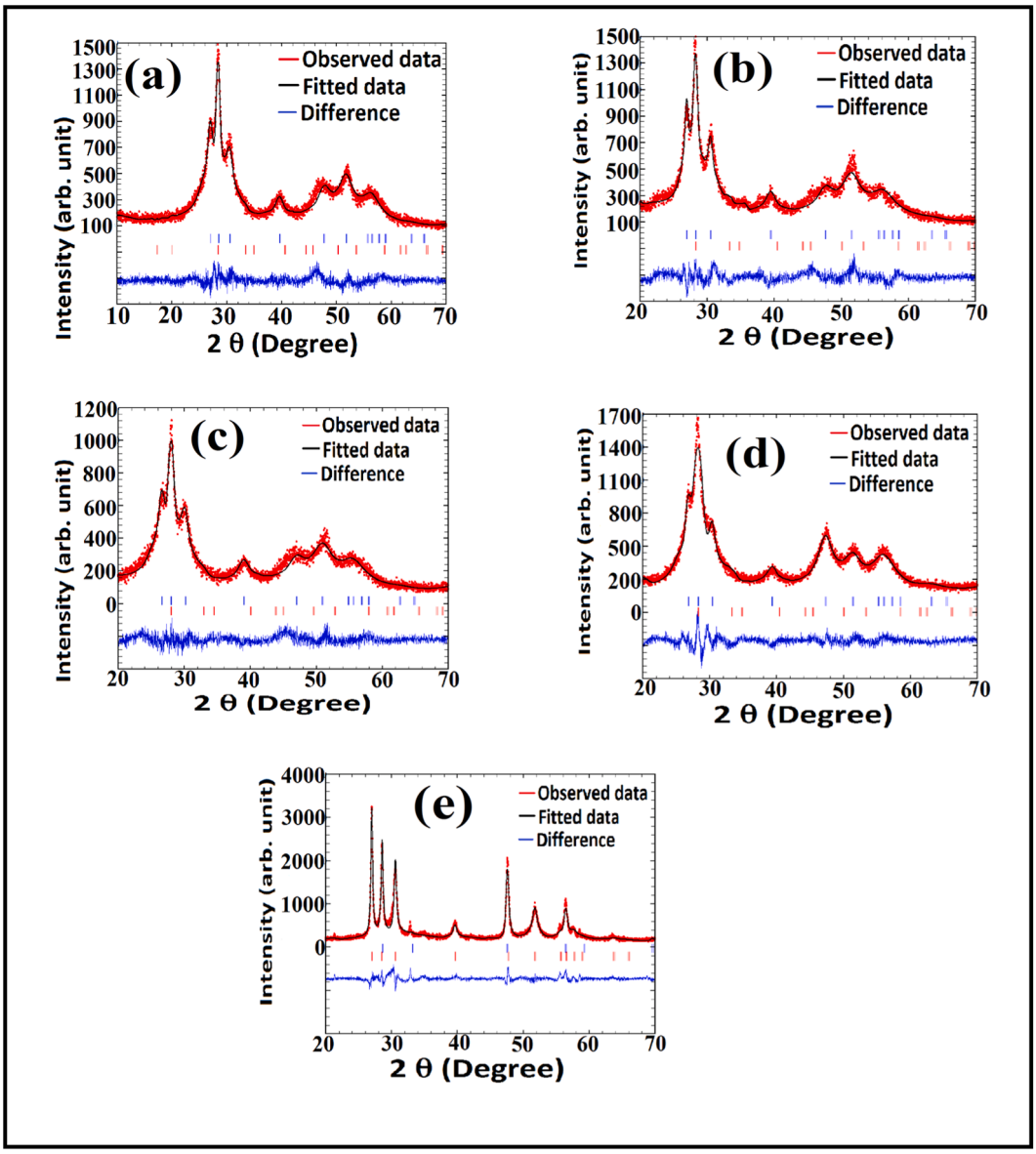

Fig. 2. Reitveld refinement of XRD pattern of ZnS having wurtzite Phase: (a)ZnS, (b)Mn, (c)Co, (d)Cd, (e)Cu doped ZnS.

Table 1
The goodness of fit, % of phases present, Lattice parameter, and Values of R factor as calculated from Rietveld refinement of XRD pattern.

Dopants (Ionic radii)		ZnS (0.82)	Mn (0.91)	Cd (1.03)	Co (0.8)	Cu (0.7)
Goodness of fit (χ)		1.63	1.74	1.54	1.71	2.06
% of phases present	Cubic	0.46 %	0.18 %	0.16 %	3.36 %	42.90 %
	Wurtzite	99.54 %	99.82 %	99.84 %	96.64 %	57.10 %
Lattice parameter	Cubic	8.89	8.93	9.01	8.93	5.41
	Wurtzite	3.82, 6.28	3.82, 6.31	3.87, 6.37	3.84, 6.32	3.81, 6.27
R_p		11.8	14.9	13.3	14	19.1
R_{wp}		14.6	17.3	16.3	16.7	19.9
R_{exp}		8.97	9.95	10.59	9.72	9.64

tabulated in Table 3.

Zinc blende ZnS have its place in T_d (43 m) point group. It has two atoms per unit cell and three-fold optic branches degenerate at $k = 0$. The degeneracy breaks immediately away from the center of the Broullian Zone (BZ). The polarization field in ionic and partially ionic crystals is a cause for such a breakdown. Thus in ZnS having a partial ionic nature, expected one LO and one TO mode at $k = 0$ both of which are Raman active. The two modes i.e. TO and LO modes near the BZ center are localized at 278 cm^{-1} and 351cm^{-1} [36,37].

In our experiment TO mode is observed at 263 cm^{-1} along with its phonon combinations i.e. $2TA_x$, and $[TO+TA]_x$ at 176 cm^{-1} and 393 cm^{-1} respectively at room temperature. LO mode is not observed but its phonon combination $[LO+TA]_x$ at 431 cm^{-1} is present in our experiment at room temperature. Overtone scattering of TO and LO is also illustrated as 2TO and 2LO at 523 cm^{-1} and 683 cm^{-1}, respectively.

"Wurtzite phase belongs to space group C_{6v} (6 mm) with 2 formula units in a primitive cell. The zone-center optical phonons can be classified as the following irreducible representations:

$$\Gamma'_{opt} = A_1 + E_1 + 2E_2 + 2B_1 \quad (3)$$

Where, B_1 modes are silent modes, A_1 and E_1 modes are polar modes and both Raman and infrared active, and E_2 modes are nonpolar and Raman active only." [36,38]

In our experiment, similar to the cubic phase, in wurtzite phase also

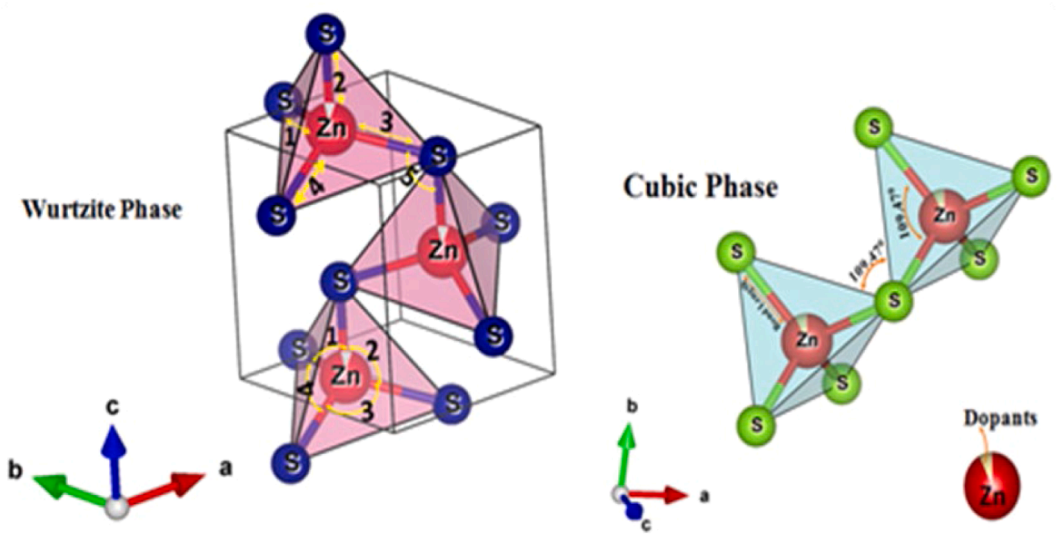

Fig. 3. Crystal structure of doped ZnS having Wurtzite structure synthesized by Conventional Coprecipitation Method.

Table 2
Bond lengths and Bond angles obtained from crystal structure.

ZnS nanostructures			ZnS	ZnS:Mn	ZnS:Cd	ZnS:Co	ZnS:Cu
Cubic	Bond length A°		3.85	3.86	3.90	3.87	2.34
Wurtzite	Bond length A°	2	2.40	2.41	2.43	2.41	2.23
		1,3,4	2.32	2.33	2.35	2.34	2.38
	Bond Angle	1,2	108.42°	108.67°	108.61°	108.58°	112.33°
		3,4	110.5°	110.26°	110.32°	110.35°	106.47°
	Bridging Angle	5	108.42°	108.67°	108.61°	108.58°	112.33°

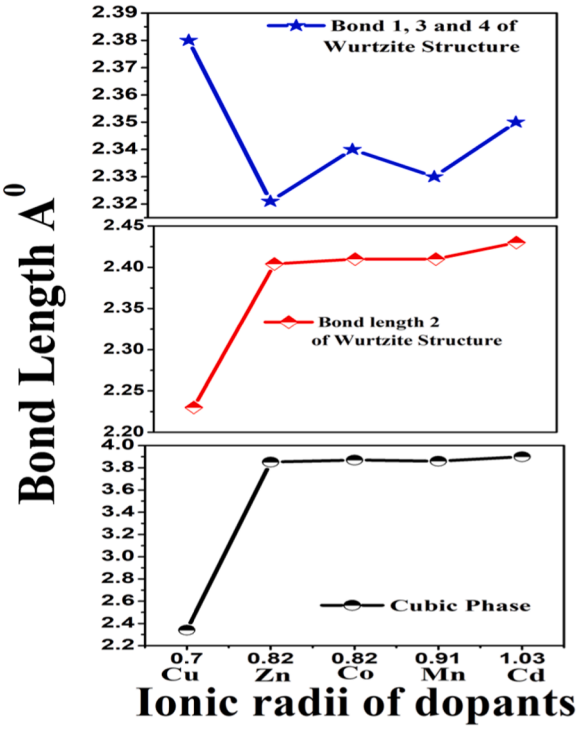

Fig. 4. Ionic radii of dopants vs bond Length.

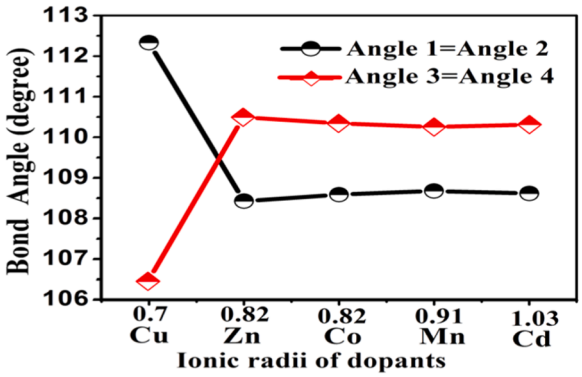

Fig. 5. Ionic radii of dopants vs bond Angle.

exhibits TO mode observed at 252 cm^{-1}, along with its phonon combinations i.e. $2TA_x$, and $[TO+TA]_x$ at 169 cm^{-1} and 391 cm^{-1} respectively at room temperature, which are slightly red-shifted compared to Cubic ZnS. In Wurtzite ZnS E_2(TO) mode is also seen. In this case, also LO mode is not observed but its phonon combinations i.e. $[LO+TA]_x$ and one extra to that of cubic ZnS i.e. $[LO+TA]_L$ at 432 cm^{-1} and 475 cm^{-1} respectively are present in our experiment at room temperature. $[LO+TA]_x$ is seen to be blue-shifted compared to cubic ZnS. Overtone scattering of TO and LO is also illustrated as 2TO and 2LO at 517 cm^{-1} and 660 cm^{-1} respectively, which are also red-shifted compared to cubic ZnS. SO Raman band associated with the surface of the nanoparticles is also observed for both the ZnS structure (Cubic and Wurtzite); indicating the non-smooth surface of the particles. Due to symmetry-breaking mechanism associated with the surface, this SO Raman band is stimulated. SO Raman band of Wurtzite ZnS (at 315 cm^{-1}) is also red-shifted equated to that of Cubic ZnS (at 335 cm^{-1}).

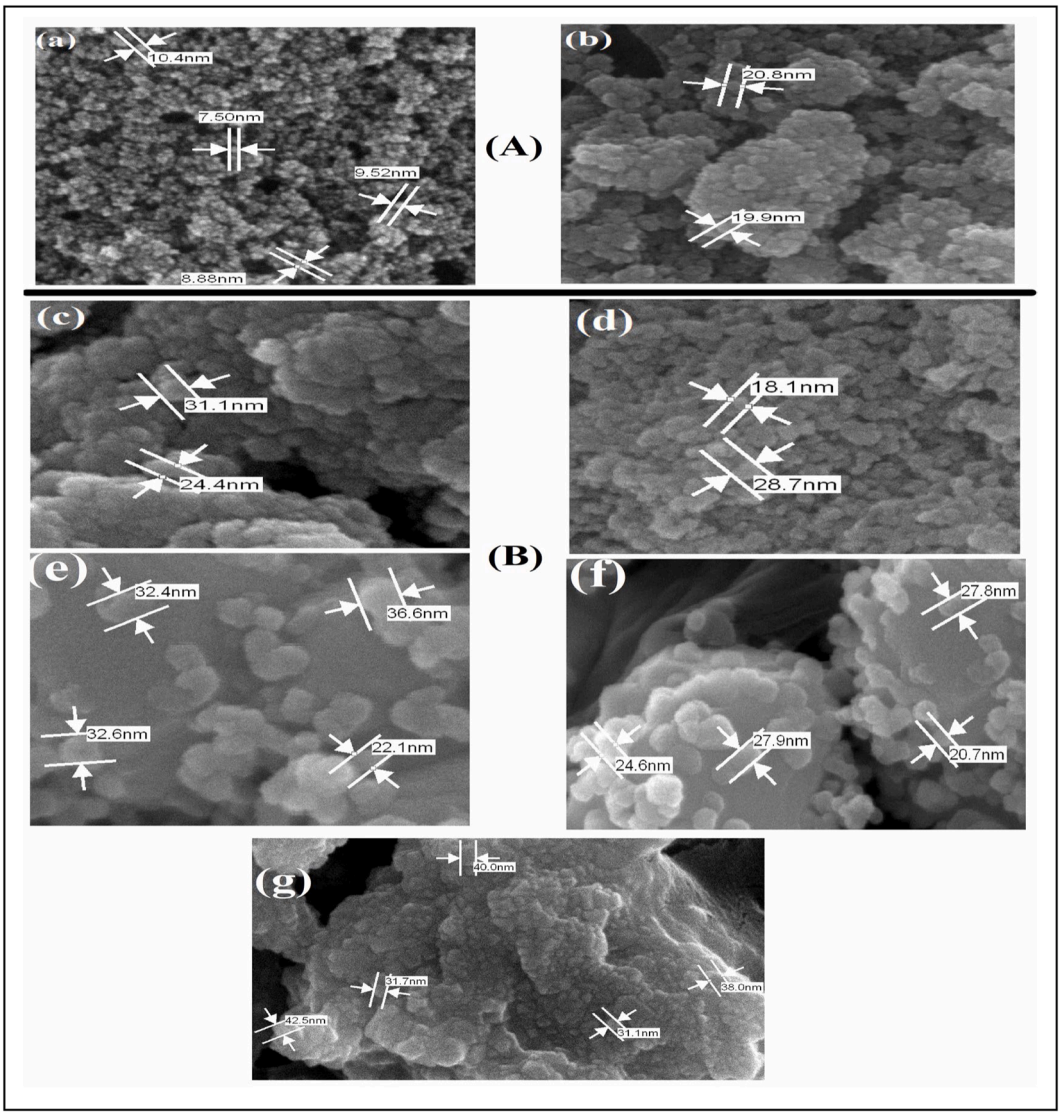

Fig. 6. SEM of **(A) cubic**: (a) ZnS (b) Mn doped ZnS **(B) Wurtzite**: (c) ZnS (d) Mn (e) Co (f) Cd and (g) Cu doped ZnS.

3.4. UV–Vis absorption spectroscopy studies

UV–Vis absorbance spectrums of freshly prepared colloidal particles of pure and doped ZnS in both the phases (i.e. Cubic and Wurtzite) are shown in Fig. 9. Fig. 9(A) exhibits UV–Vis absorption spectrum of ZnS samples having a Cubic Phase. All the spectrum exhibits an excitonic peak center at around 330 ± 8 nm. It indicates that dopands are unable to produces much detectable absorbance edge shift by dopants. There are about 12 nm of blue shift from the bulk counterparts (λ= 340 nm, E_g = 3.66 eV). This can be attributed to the quantum confinement effect of photogenerated electron-hole pairs [42,43].

In the case of ZnS having a Wurtzite phase, an absorption anomaly around 320±10 nm with redshift in the UV–Vis spectra is observed with doping as compared to the pure ZnS samples [Fig. 9(B)]. However, all the ZnS samples have a clear blue shift as compared to their bulk counterparts. There are blue shifts of about 10 nm from the bulk counterparts (λ= 330 nm, E_g = 3.77 eV). The absorption process chiefly resembled with the transmission from the valence band to the conduction band. Thus, band gap of the material can be determined with the of this process. The data obtained from the UV–Vis absorption study is tabulated in Table 4.

3.5. Photoluminescence study

In order to reveal the efficiency of electron-hole pair trapping, immigration, and transfer within semiconductor particles, Photoluminescence emission (PL) is a suitable technique. Fig. 10. illustrates the PL emissions spectra of all ZnS samples. Fig. 10**(A)** displays the PL emissions spectra of both doped and undoped ZnS samples with a Cubic Structure, while Fig. 10**(B)** exhibits the spectra for samples with a wurtzite structure. Excitation wavelengths at **265 nm and 260 nm** for ZnS samples with cubic and wurtzite structures respectively. The PL emission from the undoped ZnS NPs with a cubic phase featured two peaks; a UV peak around 370 nm and a broad peak in the visible region at about 470 nm. Conversely, doped ZnS NPs with a cubic phase displayed a single peak at about 470 nm. Although no change in peak position was observed, the PL intensities varied with the dopants.

For ZnS NPs with a wurtzite phase (Fig. 10**(B))**, the emission spectra reveal two peaks; a UV peak around 370 nm and a broad peak in the visible region at approximately 470 nm for all samples (undoped and doped). A slight shift in peak position in the UV range at 370 nm was observed with dopants, along with intensity variations. But intensity variation can be seen. The valence band (V.B) of ZnS primarily consists mostly of ‘s’ and ‘p’ orbitals from sulfur while the conduction band (C.B) consists of ‘s’ states of zinc. In pure ZnS particles, four types of point

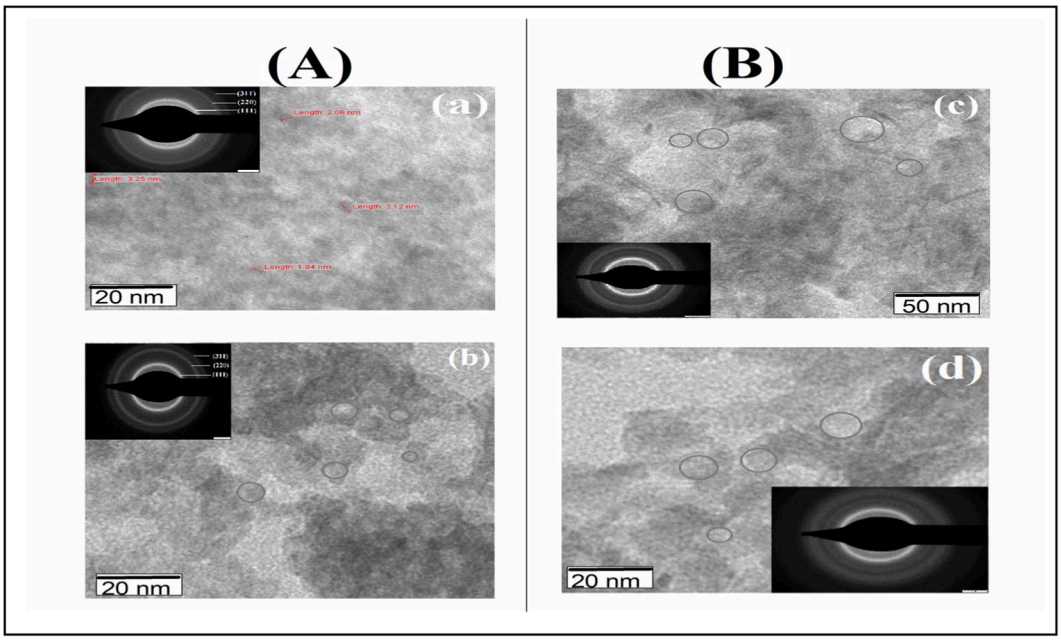

Fig. 7. TEM of **(A) Cubic**: (a) ZnS (b) Mn doped ZnS **(B) Wurtzite**: (c) ZnS and (d) Mn doped ZnS.

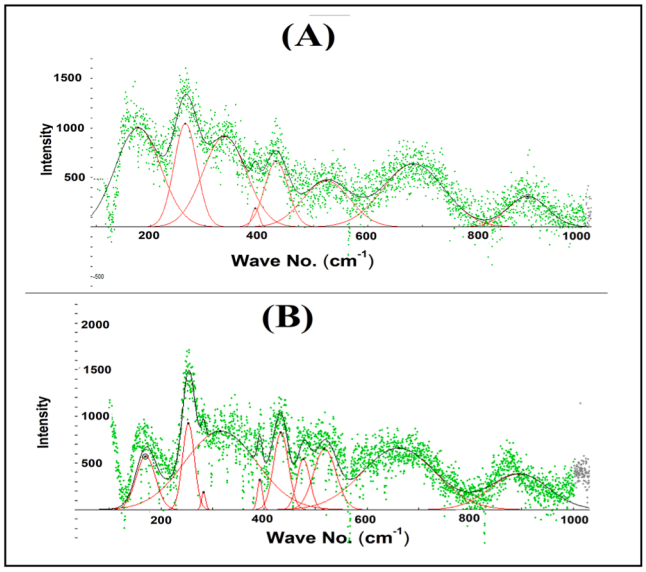

Fig. 8. Room temperature RAMAN spectra of **(A)cubic**: ZnS and **(B)Wurtzite**: ZnS

Table 3
Assignment of Raman Peaks of ZnS at room temperature.

	Frequency in(cm^{-1})		
	This Work		References
ZnS	Cubic	Wurtzite	
$2TA_x$	176.67	169.83	175 [37]
A_1/E_1(TO)	263.75	252.56 (LA)	269 [38], 267 [39], 254 [40]
E_2(TO)		281.95	282 [38]
SO	335.91	315.32	335 [38]
$[TO+TA]_x$	392.74	391.32	399 [37]
$[LO+TA]_x$	430.99	432.32	420 [37],426 [41]
$[LO+TA]_L$		475.88	450 [37]
2 TO	522.65	517.38	573 [5]
2LO	683.19	660.49	668 [40]
	892.78	894.56	

defects (sulfur vacancies, Zinc vacancies, interstitial sulfur atom, and interstitial sulfur atom) can be present. Sulfur vacancies are equivalent to localized donor and zinc vacancies to localized acceptor states. Interstitials, zinc, and sulfur atoms lead to donor and acceptor states respectively. Vacancy states lie deeper in the gap compared to states arising from interstitial atoms [23,44].

The Weak UV emission peak at 370 nm can be attributed to the near band edge emission of free excitons in the conduction band. The shifting of UV emission peaks PL spectra of doped wurtzite ZnS samples towards longer wavelength is consistent with the reduction in band gap and change in crystalline structure in the presence of dopants [23]. As there is only slight shifting in peaks observed indicates particle size remains approximately the same [14]. The emission in the blue-green region at 470 nm is attributed to a transition originating from 's' vacancies; between a shallow donor and a deep acceptor. Thus, it arises due to extrinsic and intrinsic lattice defects [44–46]. As the PL effect is a result of direct radiative recombination of electron and hole, the decrease in PL intensity is attributed to lower recombination generated carriers with dopants. In our experiment, both the structure Cu doped ZnS show lower excitonic PL intensity [45].

3.6. Photocatalytic activity

Being a surface-driven phenomenon, the surface properties of photocatalysts hold immense significance in photodegradation study. Photocatalytic activity commences at the surface of photocatalysts through photo-oxidation reactions, with the photodegradation rate contingent upon the dye's capacity to be adsorbed onto the photocatalyst's surface in the presence of light. dye to be absorbed on the surface of the photocatalyst system in the presence of light.

In the present attempt, the objective is to conduct a comparative assessment of dye photodegradation using both cubic and wurtzite ZnS under natural light conditions. Furthermore, we aim to compare the photodegradation efficacy of doped ZnS in each phase. To achieve this, we prepared suspensions of the dye (Malachite green is utilized in this study), aqueous solution, and ZnS, which were thoroughly ultrasonicated to ensure the fine dispersion of ZnS NPs in the dye solution under natural light exposure. The photodegradation of MG- ZnS system was evaluated under various conditions, including the effect of (i) Photocatalytic dosages (ii) Irradiation time, iii) different phases of ZnS

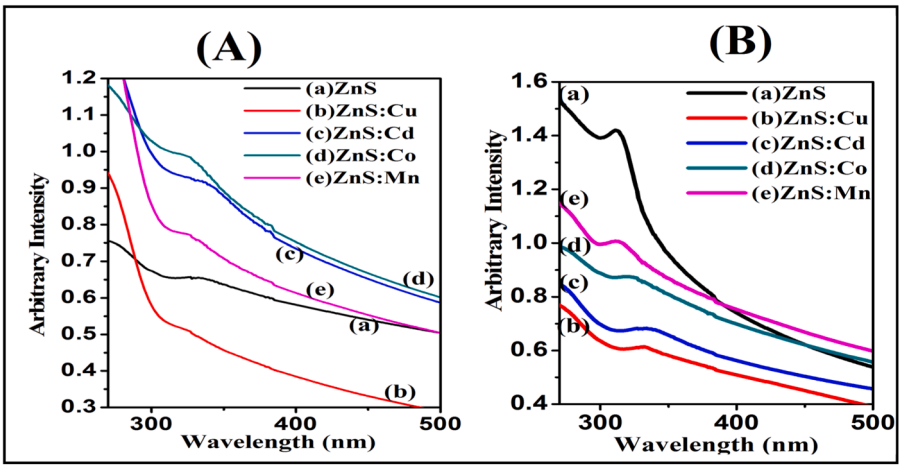

Fig. 9. UV–VIS Spectrum of **(A) Cubic:**(a)ZnS, (b)Cu, (c)Cd, (d) Co, (e) Mn doped ZnS **(B) Wurtzite:**(a)ZnS, (b)Cu, (c)Cd, (d) Co, (e) Mn doped ZnS.

Table 4
Absorption peak position and band gap calculated from UV–Vis Absorption spectra.

	Cubic		Wurtzite	
	Absorption Peak (nm)	Band Gap (eV)	Absorption Peak (nm)	Band Gap (eV)
Pure ZnS	331	3.75	311	3.997
ZnS:Mn	323	3.85	312	3.984
ZnS:Co	325	3.83	321	3.87
ZnS:Cd	332	3.74	331	3.75
ZnS:Cu	329	3.78	332	3.74

and (iv) the Effect of different dopants. The characteristic absorption of MG at 617 nm was selected as the monitored parameter for assessing the photodegradation process.

3.6.1. *Effect of doses in photodegradation*

Optimizing the doses of catalysts is crucial in photodegradation studies, as excessive use not only wastes catalysts but also renders the dye + catalyst solution opaque, thereby impeding the photodegradation rate. Beyond a certain threshold, excess particles can scatter light, resisting photodegradation rather than facilitating it.

Fig. 11 illustrates the photodegradation of MG by ZnS NPs with varying doses. Fig. 11**(A)** pertains to ZnS with a cubic phase, while Fig. 11**(B)** corresponds to the Wurtzite phase. All graphs depict a clear increase in the degradation efficiency of MG with rising catalyst doses. However, a reverse trend is observed in some samples when excessive doses are applied (inset graph). At molar concentrations of 8×10^{-3} M and 10×10^{-3} M, hindrance in the photodegradation mechanism due to excess amount of catalyst is evident for pure ZnS in both the phase [inset Fig. 11**(A) (a)** and Fig. 11**(B)** (a)].

The degradation efficiency is accredited to the priority of cleavage of the azo links in the photocatalytic degradation and decolorization, resulting in the rapid disappearance of chromophores in the dye structure.

The photodegradation efficiency is found to be strongly dependent on photocatalyst dosage (see Fig. 12).

Degradation efficiency demonstrates a direct correlation with the concentration of doses, increasing from low to higher concentrations. Achieving optimal photodegradation of dyes entails optimizing the photocatalyst concentration for a specific dopant, a parameter that varies depending on the dopant used. By examining the percentage degradation efficiency graphs of cubic and wurtzite ZnS, a threshold for photocatalyst doses conducive to optimal photodegradation can be

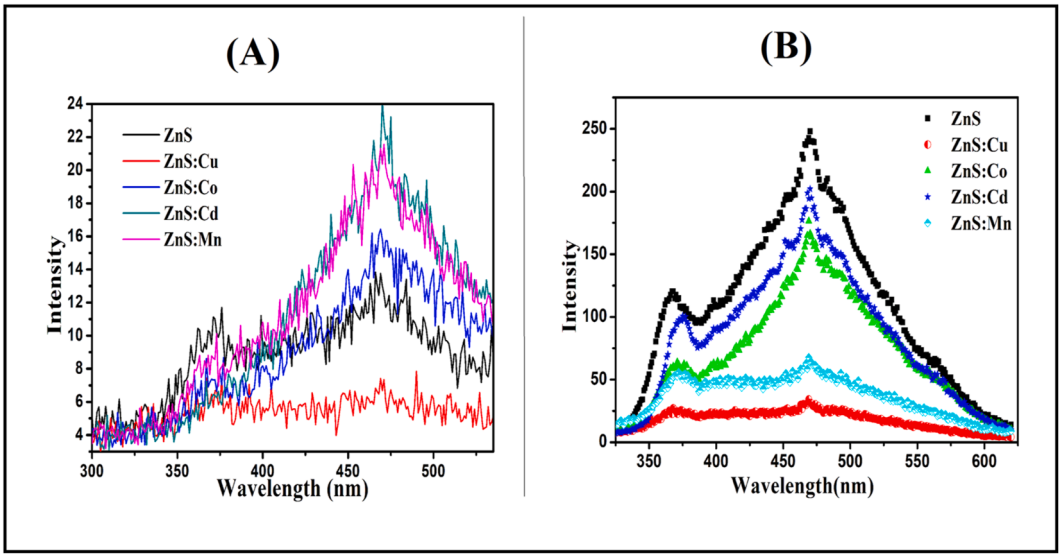

Fig. 10. PL Spectrum of **(A) Cubic:**(a)ZnS, (b)Cu, (c)Cd, (d) Co, (e) Mn doped ZnS **(B) Wurtzite:**(a)ZnS, (b)Cu, (c)Cd, (d) Co, (e) Mn doped ZnS.

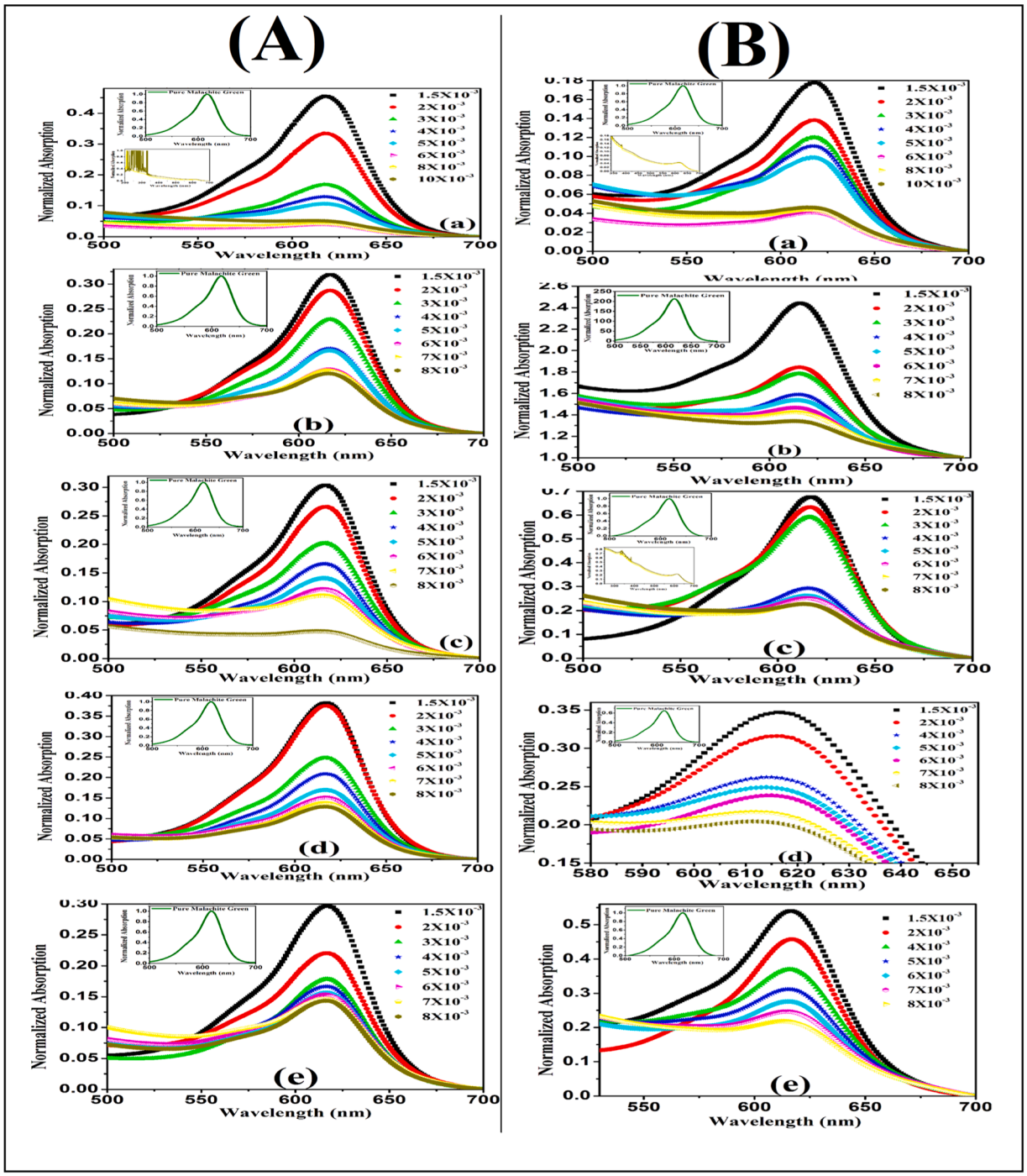

Fig. 11. Photodegradation of MG with increase in **doses** of **(A) Cubic:**(a) ZnS, (b) Mn, (c) Cd, (d) Co, (e) Cu doped ZnS **(B) Wurtzite:**(a) ZnS, (b) Mn, (c) Cd, (d) Co, (e) Cu doped ZnS.

identified.

3.6.2. *Effect of irradiation time in photodegradation*

As the photodegradation initiated with the photo-oxidation reaction, by the absorption of photons. The study of the influence of irradiation time on photodegradation is one of the most important parameters of investigation. A semiconductor like ZnS has a large band gap and thus makes its utility only in the UV domain, limiting its practical applicability in the visible regions [47]. This problem can be solved by doping of ZnS with transition metals such as Cd, Mn, Ni, Fe, Ag, etc. Doping with a transition metal, incorporates new energy levels in between the valence band (V.B.) and Conduction band (C.B.) of the host crystal lattice, shifting light absorption from UV towards VLA, along with controlled particle size and shortening lifetime from ms to ns [9–11].

Fig. 13 is the graph presenting the photodegradation of MG with the increase in the irradiation time of natural visible light. A systematic degradation of the absorption peak of MG at 617 nm with a rise in irradiation time can be observed for all samples. The time required for the complete degradation of dye is different for different catalysts. In the case of Cubic ZnS, the doped ZnS was found to be more efficient for degradation than the undoped one except Mn-doped ZnS. Co-doped ZnS require the lowest time for the complete degradation among all (doped and undoped cubic ZnS). While Mn-doped ZnS having wurtzite structure is found to be more efficient for degradation among wurtzite structure.

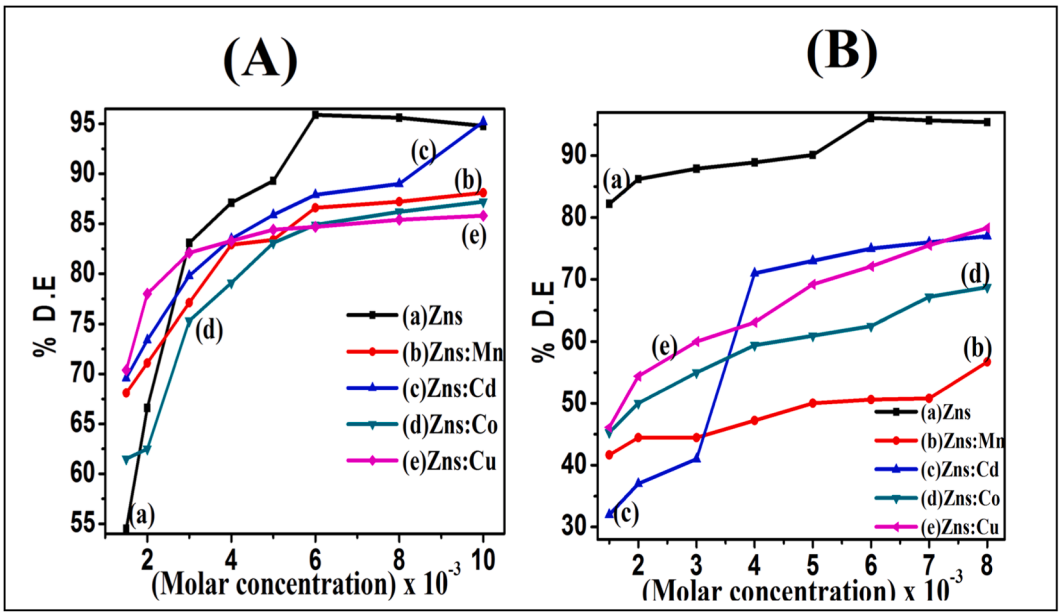

Fig. 12. Percentage degradation efficiency of MG with increase in **doses of (A) Cubic:**(a) ZnS, (b)Mn, (c) Cd, (d) Co, (e) Cu doped ZnS **(B) Wurtzite:** (a) ZnS, (b) Mn, (c) Cd, (d) Co, (e) Cu doped ZnS.

Except Mn doped Wurtzite structure all other dopants are not found to be more efficient than undoped ZnS.

The systematic comparison is further elucidated through the percentage degradation graph [Fig. 14]. It is evident that the percentage photodegradation efficiency constant is found highest for doped ZnS compared to undoped in the cubic structure. However, in the case of the Wurtzite structure, doping does not confer any advantage; in fact, it decreases efficiency compared to undoped Wurtzite ZnS. An exception is observed for Mn doping in both structures, where the percentage degradation efficiency is lowest for Mn-doped ZnS with a cubic structure but highest for Mn-doped ZnS with a wurtzite structure.

In the case of Cu-doped ZnS exhibits the lowest percentage degradation efficiency in the wurtzite structure. This could be attributed to the bulk nature of the Cu-doped wurtzite structure, possibly resulting from improper mixing of Cu in the solvent. The presence of bulk particles leads to slower degradation. The influence of the ZnS structure on the photodegradation study is evident from these findings.

In order to check the kinetics for the photocatalysis of doped ZnS, a plot of log C/Co vs time are studied. The photocatalytic reaction rate is calculated by using Pseudo first-order kinetic analysis using an equation

$$\ln\frac{C}{C_o} = -kKt = k_{obs}t \tag{4}$$

In which k_{obs} is observed first-order rate constant of the photodegradation reaction which can be calculated using the plot of $\ln(C/C_o)$ vrs *time*.

Fig. 15 depicts the graph correlating ln(Co/C) with irradiation time. The linear relationship observed upon performing a linear fit confirms the adherence to first-order decay kinetics. The calculated rate constant is tabulated in Table 4. The calculated degradation rate is in good agreement with the % D.E. However, comparing the phases, it is evident that the photodegradation rate constants are highest for both doped and undoped Cubic ZnS compared to the Wurtzite structure. An anomalous behavior is noted for Mn-doped ZnS, where the wurtzite phase exhibits higher efficiency for degradation than the cubic phase. Consequently, the overall dominance of the cubic phase in the degradation mechanism becomes apparent (Table 5).

3.6.3. *Effect of pH in photodegradation*

Any alteration to the surface of catalysts significantly impacts the photodegradation rate. The pH of the reaction solution plays a crucial role in this regard, as it leads to distinct modifications of the photocatalyst surface. This variation arises due to the isoelectric point, it is the pH at which the catalyst surface becomes neutral and carries no electric charge. pH modification affects the electrical double layer of the solid–electrote interface, influencing the sorption–desorption process. Consequently, it affects the separation of photogenerated electron-hole pairs at the photocatalyst's surface. The adsorption of dye on the surface of catalysts facilitates the transfer of electrons between the excited dye and the catalyst surface. Thereby influencing the degradation rate [47,48].

The effect of pH on the photodegradation of MG was investigated by keeping all other experimental conditions constant (i.e. concentration and volume of MG and ZnS). The initial pH value of the (ZnS+MG) solution was varied from acidic to basic, as shown in Fig. 16. It was observed that the intensity of the visible light chromophore band of MG at λ_{max} = 617 nm decreased as the pH of the solution increased.

At higher pH levels, the negatively charged surface of the photocatalysts favors the adsorption of cationic species. The occurrence of electron transfer between the excited dye and ZnS directly depends on the adsorption of the substrate onto the surface of the photocatalysts, thereby impacting the degradation rate. As the pH increases, the number of adsorption sites also increases. Additionally, the formation of hydroxyl radicals is favored in alkaline mediums. Consequently, the transfer of holes to the adsorbed ·OH radicals get improved. It enhanced the possibility of coulomb attraction between cationic dyes and negatively charged ZnS particles. These enhanced phenomEA contribute to the improved photodegradation efficiency [45,46].

3.6.4. *Effect of scavenger in photodegradation*

The reactive species (h^+or •OH) are the significant oxidizing agent in photocatalytic degradation of toxic dye. It degrades the dye pollutant by breaking the dye molecule into smaller products. In order to understand the engrossment of these active species in photocatalytic degradation mechanism, scavenger was introduced under visible light. To evaluate the contribution of reactive species, hydrogen peroxide has been used as scavenger. Hydrogen peroxide works in dual way depending on its concentration in dye + catalysts solution.

The rate of photocatalytic degradation of MG dye catalyzed by ZnS nanoparticles in presence of hydrogen peroxide is shown in Fig. 17. The

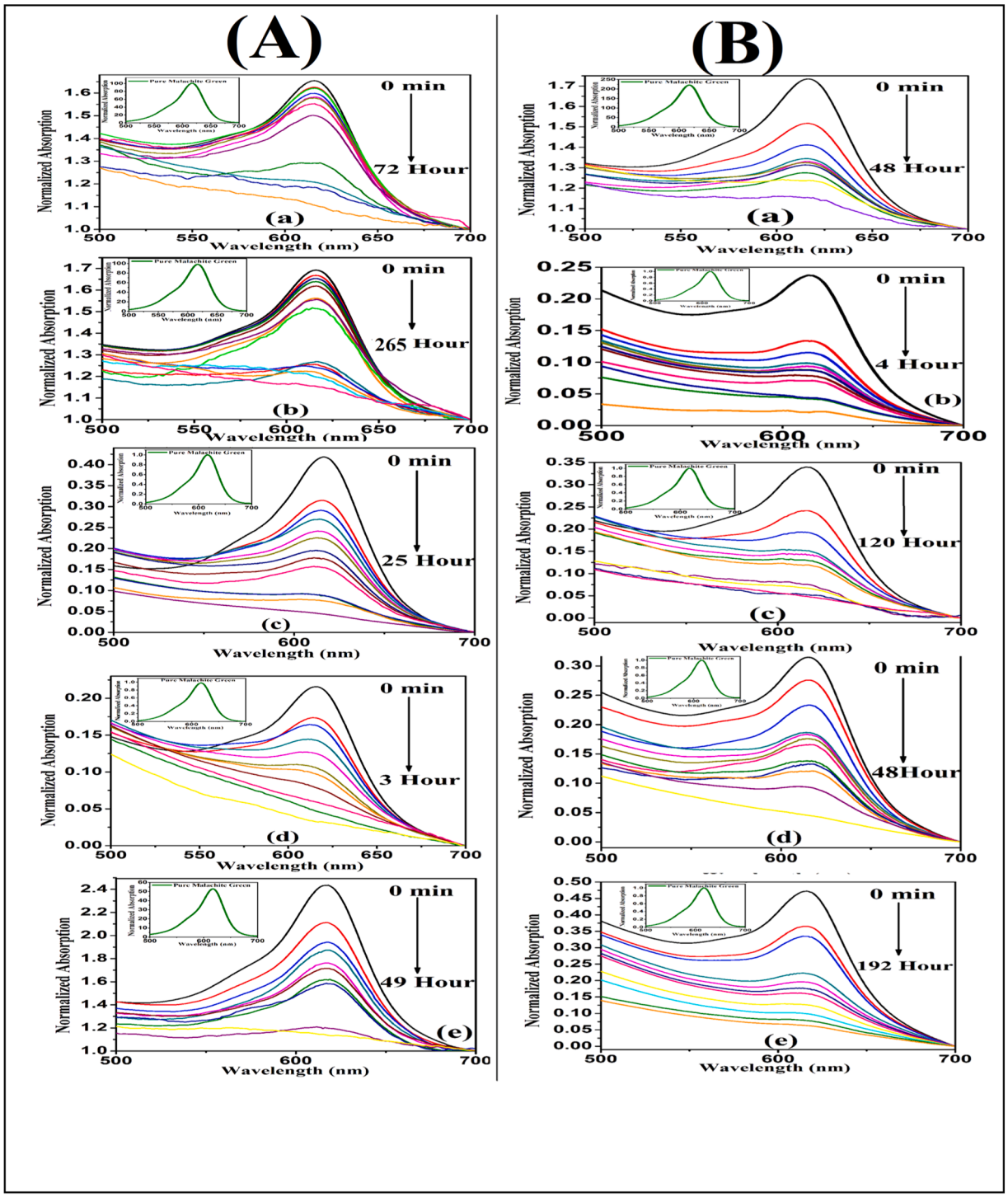

Fig. 13. Photodegradation of MG with increase in **Time** of mixed solution of MG + ZnS **(A) Cubic:**(a)ZnS, (b)Mn, (c) Cd, (d) Co, (e) Cu doped ZnS **(B) Wurtzite:**(a) ZnS, (b)Mn, (c) Cd, (d) Co, (e) Cu doped ZnS.

investigation is done for two different concentrations of H_2O_2 keeping other experimental parameters like molar concentration of catalysts, irradiation time and pH of the reaction solution constant. The percentage degradation efficiency obtained from the study is plotted for undoped and doped ZnS NPs and in both of its structures.

The percentage degradation efficiency upsurges in presence of H_2O_2 at 500mg/L than in its absence. At this concentration it behaves like electron scavenger producing more •OH on light absorption and accelerate the reaction. While at higher H_2O_2 concentration (700mg/L) it behaves like hole or •OH scavenger producing perhydroxyl radical •HO_2 which is weaker oxidant as compared to •OH. Thus at 700mg/L concentration of H_2O_2 , percentage degradation efficiency decreases even in presence of H_2O_2.

3.6.5. *Photodegradation mechanism of MG*

The photocatalytic degradation of MG dye initiates with the illumination of ZnS, a non-toxic semiconductor catalyst, with a light of an appropriate wavelength and energy (hυ) equal to or greater than the band gap energy of the semiconductor. Upon absorption of such photon,

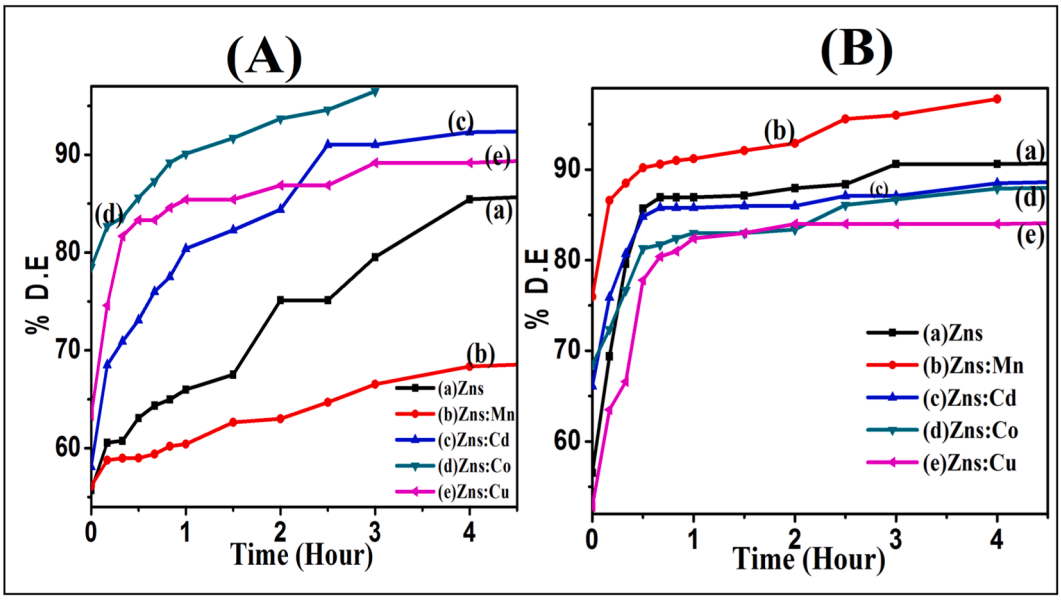

Fig. 14. Percentage degradation efficiency of MG with increase in **Irradiation Time (visible)** of mixed solution of MG + ZnS **(A) Cubic:**(a) ZnS, (b) Mn, (c) Cd, (d) Co, (e) Cu doped ZnS **(B) Wurtzite:** (a) ZnS, (b) Mn, (c) Cd, (d) Co, (e) Cu doped ZnS.

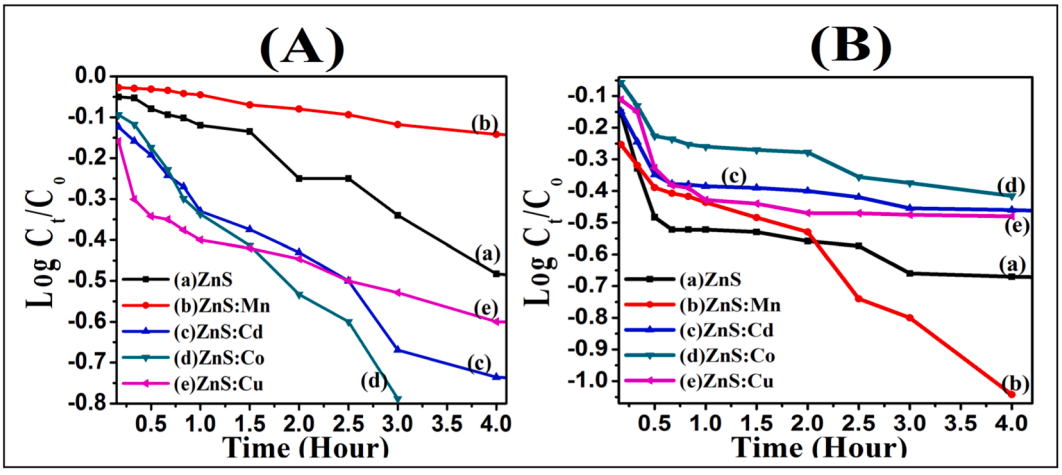

Fig. 15. Kinematics of **(A) Cubic:**(a)ZnS, (b)Mn, (c) Cu, (d) Co, (e) Cd doped ZnS **(B) Wurtzite:**(a)ZnS, (b) Cu, (c) Cd, (d) Co, (e) Mn doped ZnS.

Table 5
First order decay kinetics (k).

	Cubic	Wurtzite
Pure ZnS	−0.1017	−0.091
ZnS:Mn	−0.032	−0.185
ZnS:Cd	−0.159	−0.051
ZnS:Co	−0.229	−0.069
ZnS:Cu	−0.106	−0.029

the electrons from filled valence band electrons (from the highest occupied molecular orbital, HOMO) become excited and transition to the empty conduction band (lowest unoccupied molecular orbital, LUMO) leaving a hole behind [50,51]. This charge separation results in the formation of a reactive electron-hole pair, which then migrates separately to the semiconductor/water interface to participate in redox reactions with surrounding species.

These reactions generate. OH radicals, which play a pivotal role in the degradation of pollutants within the medium, convert most of the toxic organic material into degradation products along with carbon dioxide and water. Importantly, the photocatalyst remains intact and is not consumed during the process [50,52]. The formation of .OH radicals by electrons and holes take place via two routes.

1) Oxidative reactions due to holes in photocatalytic effect, wherein valence band "holes" (h^+_{vb}) react either with adsorbed H_2O or with the surface OH^- groups on the ZnS nanoparticle.
   (i) $ZnS(h^+_{vb}) + H_2O_{ads} \rightarrow ZnS + {}^{\bullet}OH_{ads} + H^+$ or
   $2\,h^+ + 2\,H_2O \rightarrow 2\,H^+ + H_2O_2$
   $H_2O_2 \rightarrow HO^{\bullet} + {}^{\bullet}OH$
   (ii) $ZnS(h^+_{vb}) + OH_{ads} \rightarrow ZnS + {}^{\bullet}OH_{ads}$
2) In the photocatalytic effect, reductive reactions occur due to electrons, with oxygen playing a crucial role. Oxygen can trap conduction-band electrons to form superoxide ions ($^{\bullet}O_2^-$). These superoxide ions can react with hydrogen ions (formed by splitting water), to produce hydrogen peroxide (H_2O_2).

$$e^- + O_2 \rightarrow \bullet O^{2-}$$

$$\bullet O^{2-} + 2H^+ \rightarrow H_2O_2$$

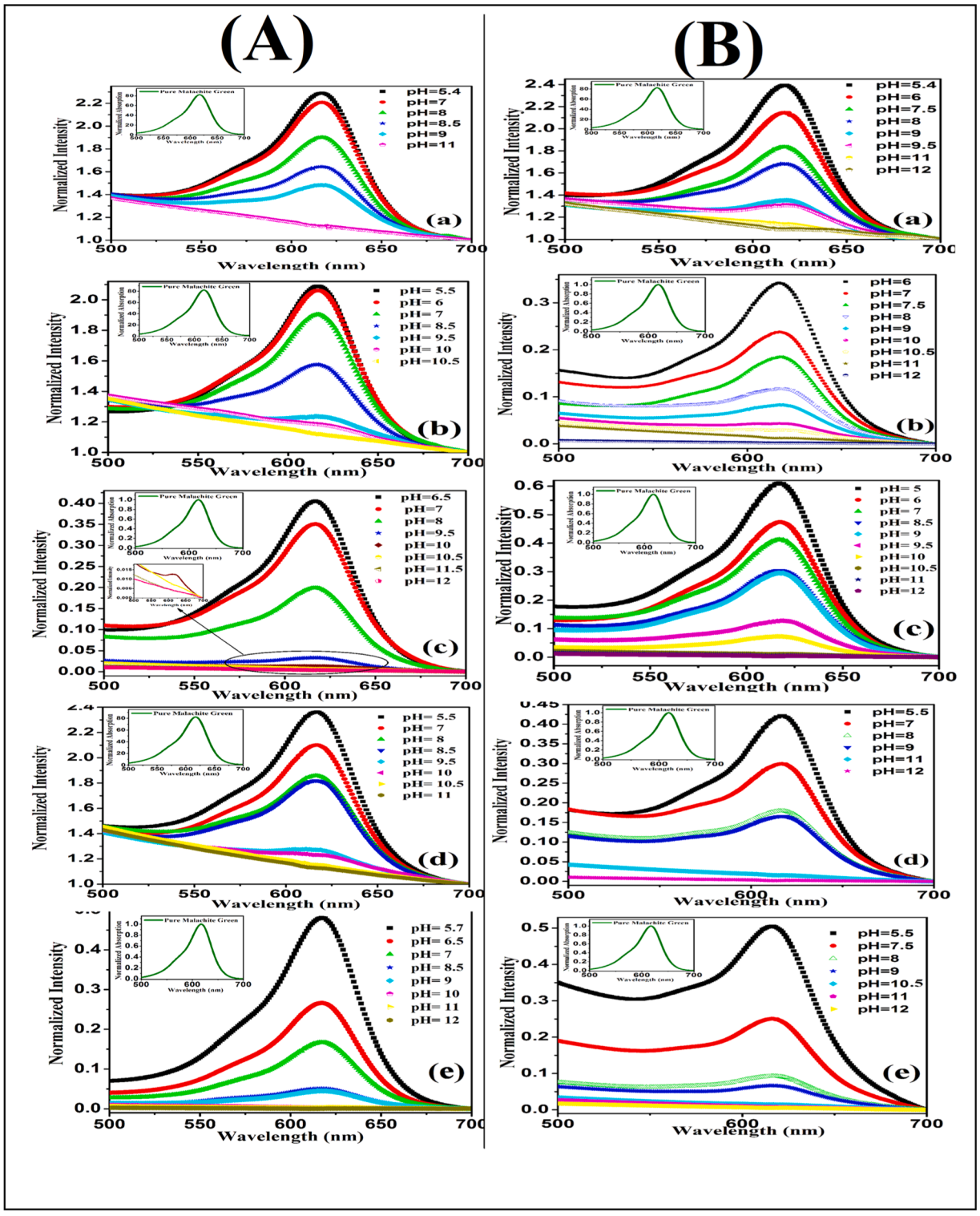

Fig. 16. Photodegradation of MG with increase in **pH** of mixed solution of MG + ZnS **(A) Cubic:**(a)ZnS, (b)Mn, (c) Cd, (d) Co, (e) Cu doped ZnS **(B) Wurtzite:**(a)ZnS, (b)Mn, (c) Cd, (d) Co, (e) Cu doped ZnS.

Cleavage of H_2O_2 by one of the reactions below may yield an •OH radical.

$H_2O_2 + h\nu \rightarrow 2\ \bullet OH$

$H_2O_2 + \bullet O^{2-} \rightarrow \bullet OH + O_2 + OH^-$

$H_2O_2 + ZnS(e^-_{CB}) \rightarrow ZnS + \bullet OH + OH^-$

Finally, these hydroxyl species along with direct hole attack dye result into its degradation products with the evolution of CO_2 and H_2O.

$h^+_{vb}(ZnS) + dye \rightarrow dye\bullet +$ oxidation of the dye

$\bullet OH_{ads} + dye \rightarrow$ degradation of the dye $+ CO_2 + H_2O$

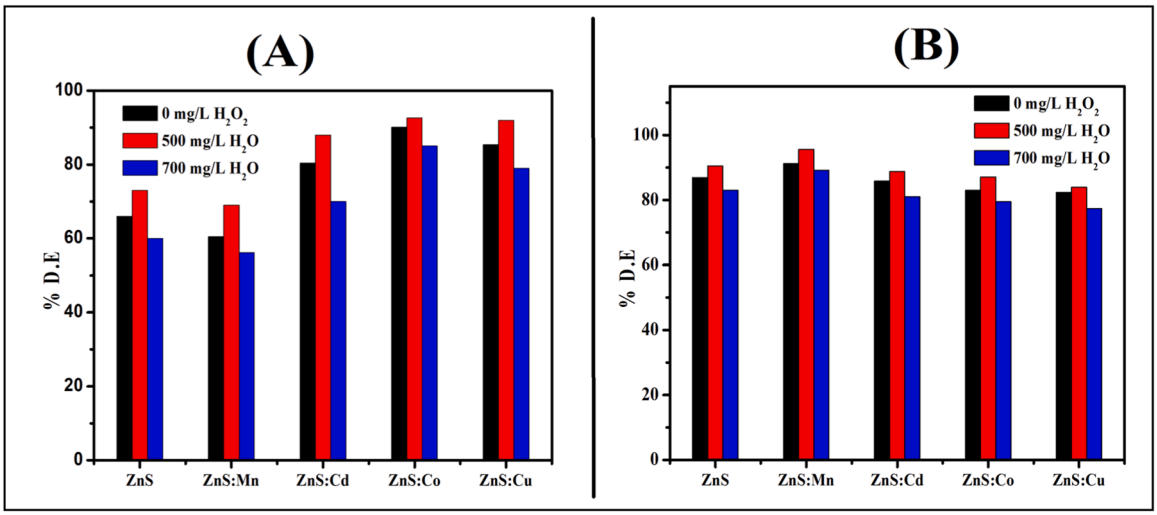

Fig. 17. Scavengers of **(A) Cubic:**(a)ZnS, (b)Mn, (c) Cu, (d) Co, (e) Cd doped ZnS **(B) Wurtzite:**(a)ZnS, (b) Cu, (c) Cd, (d) Co, (e) Mn doped ZnS.

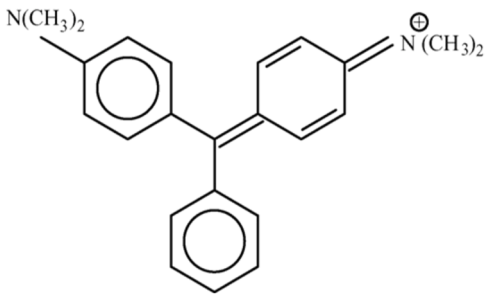

Fig. 18. Chemical structure of Malachite green (MG) dye **[**49**]**.

In the photocatalysis process, the role of dopant concentration is crucial as it influences photo redox chemistry occurring at the surface of nanocrystals through trapped charge carriers. Acting as a trap for electrons or holes is the primary function of a dopant. When dopants are Incorporated into the ZnS crystal structure, they introduce various localized energy states within the forbidden energy gap of ZnS. The localized energy levels play a significant role in charge carrier recombination and trapping processes. The competition between charge carrier trapping and recombination ultimately determines the surface charge transfer, which is essential for photo-redox reactions. If the dopant acts as a trap for electrons, it creates an easy path for holes to transfer to the semiconductor surface and react with OH^- in the dye solution, generating active $OH^·$ hydroxyl radicals involved in the degradation of the dye.

The process of charge trapping is as follows-

$$Photocatalysts + h\nu \rightarrow Photocatalysts\ (e^-_{CB} + h^+_{VB})$$

$$M^{n+} + e^- \rightarrow M^{(n-1)+}(\text{Reduction})$$

$$M^{(n-1)+} + O_2 \rightarrow M^{(n-1+1)+} + O_2^-$$

$$M^{n+} + h^+ \rightarrow M^{(n+1)+}(\text{Oxidation})$$

$$M^{(n+1)+} + OH^- \rightarrow M^{(n+1-1)+} + OH^·$$

$M^{n+}/\ M^{(n-1)+}$ → lies below C.B

$M^{n+}/\ M^{(n+1)+}$ → lies above V.B

Where M is the dopant ion, n is the valency of the dopant ion [53,54].

Malachite green belongs to the triphenylmethane group of commercial dyes. The chemical strcture of it is shown in Fig. 18. These dyes are well known for their vivid color intensity, brilliant shade, and low-light fastness. Through its photocatalytic activity, ZnS produces hydroxyl radicals, which are highly reactive species. These radicals oxidize the organic molecules of MG, initiating a cascade of reactions that lead to the formation of intermediate degradation products. These reactions cleave the benzene rings, converting them into simpler and less toxic molecules, ultimately resulting in complex mineralization [49,55].

Y.Ju et.al (2008) reported several open-ring intermediates, including phenol, terephthalic acid, oxalic acid, benzoic acid, terephthalic acid formate, lactic acid, along with unidentified intermediate products labeled as C (m/z = 345), H (m/z = 361), and I (m/z = 345). These intermediates further react with hydroxyl radicals to produce compounds labeled as J (m/z = 327), K (m/z = 313), and L (m/z = 299) through dehydration and *N*-demethylation reaction [49].

Similarly, A.T. Amigun et.al (2022) identified open-ring intermediates such as 4,4-(dimethylamino) phenyl](phenyl)methylidene (m/z = 315), 4-(dimethylamino)phenyl (m/z = 301), 4-(methylamino) benzophenone (m/z = 211), 4-(dimethylamino) benzophenone (m/z = 225), 1-(4-aminophenyl)ethan-1-one (m/z = 135), 1-phenylethan-1-one (m/z = 119) and final product (propan-2-one) with (m/z = 57) [55].

The degradation of MG involves three primary photooxidation pathways: (1) N-de-methylation, leading to the formation of various radicals either carbon-centred radical or nitrogen-centred radical, (2) destruction of the chromophore structure, and (3) Hydroxylation without the open- ring reaction. In our case, the degradation occurs through the destruction of the chromophore structure, as evidenced by the absence of a hypsochromic shift in the absorption peak of MG at 617 nm. The proposed degradation mechanism of MG by destruction of the chromophore structure is illustrated in Fig. 19 [49,55].

Thus, the degradation of MG is supposed to take place via series of intermediate products. Hydroxylation, demethylation, oxidation, deamination and benzene ring cleavage are the proposed reaction, occur to degrade MG dye into simple and less toxic molecule, which after further degradation leads to mineralization of MG dye.

4. Conclusion

In Summary, ZnS in both of its phases has been synthesized by the co-precipitation route. With ethanolamine as a soft template, the phase transformation temperature of ZnS has been reduced to a low temperature (120 °C). XRD and SAED confirm single phase zinc blende structure of as-synthesized ZnS in the absence of ethanolamine while the wurtzite phase of ZnS in the presence of ethanolamine. SEM and TEM images show particles sizes of as-synthesized cubic ZnS are in the range

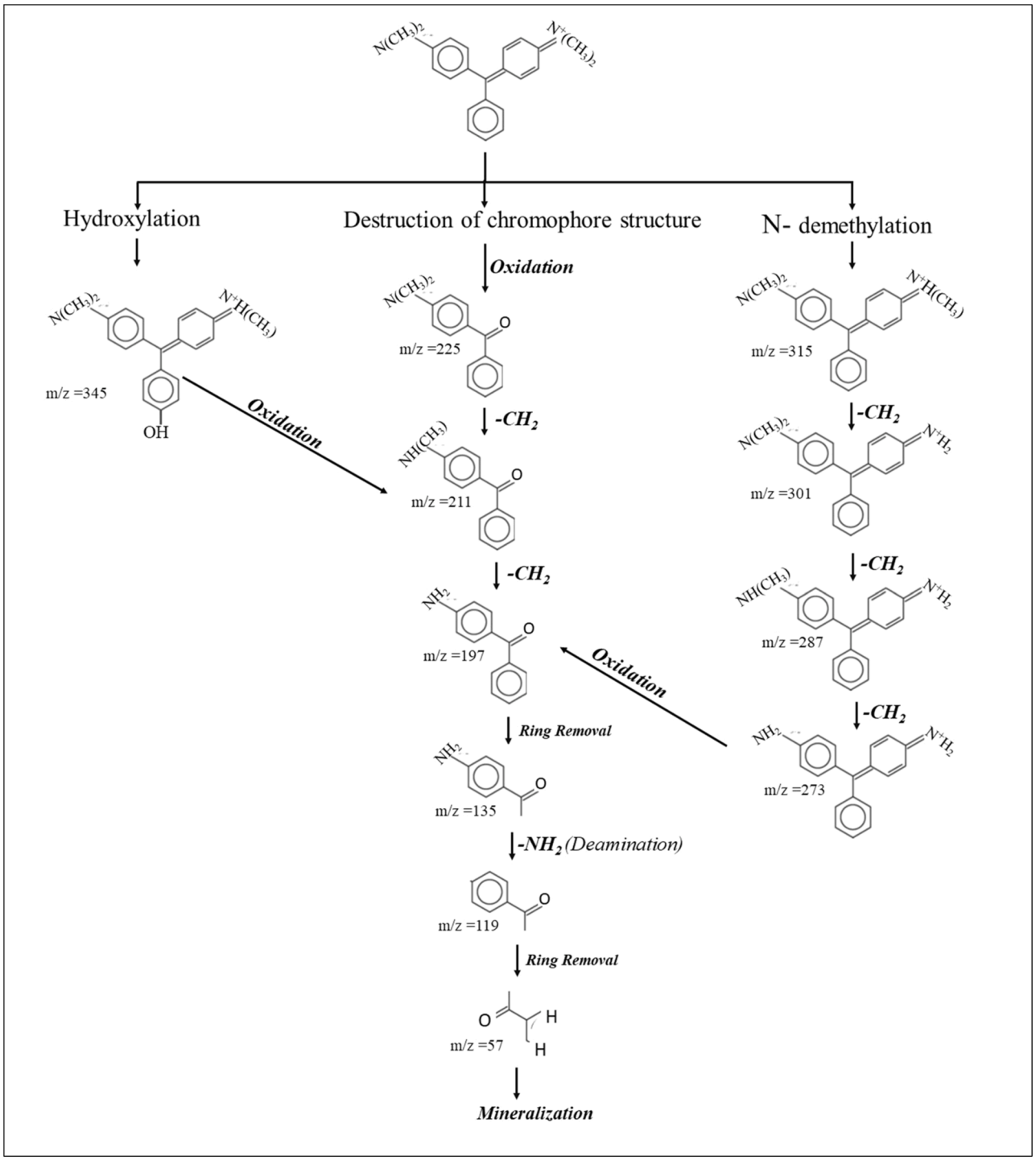

Fig. 19. Proposed degradation mechanism of MG.

of 20 to 40 nm. The blue shift in UV–Vis absorption spectra of as-synthesized (cubic and wurtzite) ZnS can be seen. The potential of as-synthesized samples is investigated by studying the photodegradation of Malachite green by adding different molar proportional of (cubic and wurtzite) ZnS in the dye; until the complete de-coloration of dyes. Also, the potential is investigated for the well-ultrasonicated mixture of MG + ZnS with exposed time intervals. The rate of de-coloration of dye is detected by UV–VIS absorption spectroscopy. The effect of pH on the mixture of MG + ZnS was studied. A very small concentration in the range of mg/L proportion is needed for complete photodegradation of the dyes as compared to bulk counterpart 10^{-2} g/L. The dependency of photodegradation of dye pollutants on the structure of ZnS can be clearly understood. Doped ZnS samples in both of its phases (Cubic and Wurtzite) are more efficient for the photodegradation of toxic dyes than the undoped one. Undoped and Mn doped ZnS having Wurtzite Phase are superior degradation efficiency of doped Wurtzite ZnS for Malachite green dye, highlighting its potential for environmental remediation applications.

CRediT authorship contribution statement

Rohini A. Khaparde: Writing – review & editing, Writing – original

draft, Visualization, Supervision, Methodology, Investigation, Formal analysis, Data curation, Conceptualization. **Smita A. Acharya:** Supervision, Conceptualization, Writing – review & editing. **Priya Tumram:** Visualization, Data curation. **Shahin Sayyed:** Investigation.

Declaration of competing interest

The author declare that they have no know competing financial interests or personal relationships that could have appeared to influence the work reported in this paper.

Acknowledgement

The authors want to acknowledge UGC-DAE-CSR- Indore centre for extending the Raman spectroscopy facility to conduct this work.

Data availability

Data will be made available on request.

References

[1] Y. Ding, X.D. Wang, Z.L. Wang, Phase controlled synthesis of ZnS nanobelts: zinc blende vs wurtzite, Chem. Phys. Lett 398 (2004) 32–36, https://doi.org/10.1016/j.cplett.2004.09.031.
[2] T. Kuzuya, Y. Tai, S. Yamamuro, K. Sumiyama, Size-focusing of ZnS nanocrystals observed by MALDI-TOF mass spectroscopy, Chem. Phys. Lett 407 (2005) 460–463, https://doi.org/10.1016/j.cplett.2005.03.114.
[3] S.B. Qadri, E.F. Skelton, D. Hsu, A.D. Dinsmore, J. Yang, H.F. Gray, B.R. Ratna, Size-induced transition-temperature reduction in nanoparticles of ZnS, Phys. Rev. B. Condens. Matter. Mater. Phys 60 (1999) 9191–9193, https://doi.org/10.1103/PhysRevB.60.9191.
[4] S.R. Walsh, I. Rusakova, K.H. Whitmire, Rock salt vs. wurtzite phases of Co1-xMnxO: control of crystal lattice and morphology at the nanoscale, CrystEngComm 15 (2013) 775–784, https://doi.org/10.1039/c2ce26440d.
[5] M. Moffitt, A. Eisenberg, Size control of nanoparticles in semiconductor-polymer composites. 1. control via multiplet aggregation numbers in styrene-based random ionomers, Chem. Mater 7 (1995) 1178–1184, https://doi.org/10.1021/cm00054a017.
[6] R. Shahid, Microwave-assisted low temperature synthesis of wurtzite ZnS quantum dots, (2012). https://doi.org/10.1016/j.jssc.2012.01.007.
[7] F.P. Ramanery, A.A.P. Mansur, H.S. Mansur, Synthesis and characterization of water-dispersed CdSe/CdS core-shell quantum dots prepared via layer-by-layer method capped with carboxylic-functionalized poly(vinyl alcohol), Mater. Res 17 (2014) 133–140, https://doi.org/10.1590/S1516-14392014005000060.
[8] J.O. Diaz-Reyes, Castillo-Ojeda, R.S.; Sanchez-Espindola, R.; Galvan-Arellano, M.; Zaca-Moran, structural and optical characterization of wurtzite type ZnS n, 15 (2015) 103–109. https://doi.org/10.1016/j.cap.2014.11.012.
[9] P. Sakthivel, R.V. Mangalaraja, G. Ramalingam, K. Sakthipandi, V. Gowtham, Synthesis, structure, morphology, element composition, electrochemical, and optical studies of Zn0.98-XMn0.02CeX quantum dots, Spectrochim. Acta. A. Mol. Biomol. Spectrosc 303 (2023), https://doi.org/10.1016/j.saa.2023.123140.
[10] R. Khaparde, S. Acharya, Effect of isovalent dopants on photodegradation ability of ZnS nanoparticles, Spectrochim. Acta. A. Mol. Biomol. Spectrosc 163 (2016) 49–57, https://doi.org/10.1016/j.saa.2016.03.025.
[11] M. Mb, L. Pb, Effect of Cd and N doping on Zinc sulphide nanoparticles synthesised by mechanochemical method for the photodegradation of brilliant green dye, Nano. Res. Applic 5 (2019) 1–7, https://doi.org/10.36648/2471-9838.5.1.38.
[12] F. Yang, N.N. Yan, S. Huang, Q. Sun, L.Z. Zhang, Y. Yu, Zn-doped CdS nanoarchitectures prepared by hydrothermal synthesis: mechanism for enhanced photocatalytic activity and stability under visible light, J. Phys. Chem. C 116 (2012) 9078–9084, https://doi.org/10.1021/jp300939q.
[13] R. Chauhan, A. Kumar, R. Pal Chaudhary, Photocatalytic degradation of methylene blue with Cu doped ZnS nanoparticles, J. Lumin 145 (2014) 6–12, https://doi.org/10.1016/j.jlumin.2013.07.005.
[14] P. Sakthivel, S. Muthukumaran, Structural, photoluminescence and magnetic properties of Mn, Cr dual-doped ZnS quantum dots: influence of Cr concentration, J. Phys. Chem. Solids 120 (2018) 183–189, https://doi.org/10.1016/j.jpcs.2018.04.037.
[15] B. Abdallah, M. Kakhia, N. Alkafri, Investigation of ZnS nanotubes films: morphological, structural and optical properties, J. Nano Res. 60 (2019) 142–153, https://doi.org/10.4028/www.scientific.net/JNanoR.60.142.
[16] B. Abdallah, M. Kakhia, W. Zetoune, Structural, optical and sensing properties of ZnS thick films deposited by RF magnetron sputtering technique at different powers, World J. Eng 17/3 (2020) 381–388, https://doi.org/10.1108/WJE-10-2019-0300.
[17] B. Abdallah, M. Kakhia, W. Zetoune, 1-HRTEM study of ZnS nanowires films deposited by thermal evaporation, J. Nanostruc 10 (4) (2020) 713–722, https://doi.org/10.22052/JNS.2020.04.004.
[18] V. Preethi, S. Kanmani, Photocatalytic hydrogen production using Fe2O3-based core shell nano particles with ZnS and CdS, Int. J. Hydrogen Energy 39 (2014) 1613–1622, https://doi.org/10.1016/j.ijhydene.2013.11.029.
[19] Z. Kuspanov, B. Bakbolat, A. Baimenov, A. Issadykov, Science of the total environment photocatalysts for a sustainable future : innovations in large-scale environmental and energy applications combined computational fluid dynamics, Sci. Total Environ 885 (2023) 163914, https://doi.org/10.1016/j.scitotenv.2023.163914.
[20] P. Taylor, X. Fang, Y. Bando, U.K. Gautam, T. Zhai, H. Zeng, X. Xu, M. Liao, D. Golberg, Critical reviews in solid state and materials sciences ZnO and ZnS nanostructures : ultraviolet-light emitters, lasers, and sensors ZnO and ZnS nanostructures : ultraviolet-light emitters, Laser., Sensor. (2009), https://doi.org/10.1080/10408430903245393.
[21] X. Fang, Y. Bando, U.K. Gautam, T. Zhai, H. Zeng, X. Xu, M. Liao, D. Golberg, ZnO and ZnS nanostructures: ultraviolet-light emitters, lasers, and sensors, 2009. https://doi.org/10.1080/10408430903245393.
[22] S. Murugan, M. Ashokkumar, P. Sakthivel, Preparation and characterization of ZnS: MgS nanocomposites for photocatalytic and antioxidant applications, Vacuum 215 (2023), https://doi.org/10.1016/j.vacuum.2023.112256.
[23] S. Murugan, M. Ashokkumar, P. Sakthivel, D. Choi, Sulfur deficiency mediated visible emission of ZnS QDs by magnesium dopant and their application in waste water treatment, Heliyon 9 (2023), https://doi.org/10.1016/j.heliyon.2023.e17947.
[24] A. Alharbi, R.K. Shah, A. Sayqal, A. Subaihi, A.A. Alluhaybi, F.K. Algethami, A. M. Naglah, A.A. Almehizia, H.A. Katouah, H.M. Youssef, Facile synthesis of novel zinc sulfide/chitosan composite for efficient photocatalytic degradation of acid brown 5G and acid black 2BNG dyes, Alexand. Eng. J. 60 (2021) 2167–2178, https://doi.org/10.1016/j.aej.2020.12.025.
[25] H. Soni, N. Kumar, UV light induced photocatalytic degradation of malachite green on TiO 2 nanoparticles, 2014. https://www.researchgate.net/publication/282975466.
[26] S. MeEA, D. Vaya, B.K. Das, Photocatalytic degradation of malachite green dye by modified ZnO nanomaterial, Bull. Mater. Sci 39 (2016) 1735–1743, https://doi.org/10.1007/s12034-016-1318-4.
[27] P.A. Ajibade, N. Solomane, B.M. Sikakane, Morphological studies and photocatalytic degradation of methylene blue by zinc sulfide nanoparticles, 19 (2022) 429–438.
[28] I. Ahmad, Y. Zou, J. Yan, Y. Liu, S. Shukrullah, M. Yasin, H. Hussain, W. Qamar, N. R. Khalid, Semiconductor photocatalysts : a critical review highlighting the various strategies to boost the photocatalytic performances for diverse applications, Adv. Colloid. Interface. Sci 311 (2023) 102830, https://doi.org/10.1016/j.cis.2022.102830.
[29] M.H. Baek, C.O. Ijagbemi, S.J. O, D.S. Kim, Removal of Malachite Green from aqueous solution using degreased coffee bean, J. Hazard. Mater 176 (2010) 820–828, https://doi.org/10.1016/j.jhazmat.2009.11.110.
[30] R.A. Khaparde, S.A. Acharya, Efficient photocatalytic degradation of malachite green dye under visible irradiation by water soluble ZnS:Mn/ZnS core/shell nanoparticles, AIP. Conf. Proc 1953 (2018) 1–6, https://doi.org/10.1063/1.5032474.
[31] M. Naghiloo, S.;. Habibi-Yangjeh, A.;. Behboudnia, Adsorption and photocatalytic degradation of methylene blue On Zn1-x Cux S nanoparticles prepared by a simple green method, Appl. Surf. Sci 257 (2011) 2361–2366, https://doi.org/10.1016/j.apsusc.2010.09.103.
[32] L.W. Buck, C. Daniel and Strock, Trimorphism in zinc sulfide, 2942 (1953).
[33] W. Shan, L. Hu, X. Lin, M. Chen, L. Wu, Oil-water interfacial self-assembly of PS/ZnS nanospheres and photoconducting property of corresponding nanofilm, J. Mater. Chem 22 (2012) 17671–17676, https://doi.org/10.1039/c2jm32164e.
[34] A. Upcher, V. Ezersky, A. Berman, Y. Golan, Twinning and phase control in template-directed ZnS and (Cd,Zn)S nanocrystals, Cryst. Growth. Des 13 (2013) 2149–2160, https://doi.org/10.1021/cg4002384.
[35] R.A. Khaparde, S.A. Acharya, Crystal engineering of ZnS by cationic and anionic surface capping agent-cum-solvent, Mater. Res. Express 6 (2019) 1250i6, https://doi.org/10.1088/2053-1591/ab5dd5.11.1953, 1953.
[36] Y.C. Cheng, C.Q. Jin, F. Gao, X.L. Wu, W. Zhong, S.H. Li, P.K. Chu, Raman scattering study of zinc blende and wurtzite ZnS, J. Appl. Phys 106 (2009), https://doi.org/10.1063/1.3270401.
[37] Y.T. Nien, I.G. Chen, Raman scattering and electroluminescence of ZnS:Cu,Cl phosphor powder, Appl. Phys. Lett 89 (2006), https://doi.org/10.1063/1.2423326.
[38] Q. Xiong, J. Wang, O. Reese, L.C.L.Y. Voon, P.C. Eklund, Raman scattering from surface phonons in rectangular cross-sectional w-ZnS nanowires, Nano. Lett. 4 (2004) 1991–1996, https://doi.org/10.1021/nl048720h.
[39] R. Schneider, J. Kirby, Raman scattering from ZnS polytypes, Physi. Rev. B 6 (1972) 1290–1294.
[40] S.B. Dhara; Arora, A.K.; Ghatak, Jay; Chen, K.H.; Liu, C.P.; Chen, L.C.; Tzeng, Y.; and Raj, Deformation potential dominated phonons in ZnS quantum dots, (n.d.) 1–12.
[41] J. Díaz-Reyes, R.S. Castillo-Ojeda, R. Sánchez-Espíndola, M. Galván-Arellano, O. Zaca-Morán, Structural and optical characterization of wurtzite type ZnS, Curr. Appl. Phys. 15 (2015) 103–109, https://doi.org/10.1016/j.cap.2014.11.012.
[42] Y. Chen, R. Yin, Q. Wu, Solvothermal synthesis of well-disperse ZnS nanorods with efficient photocatalytic properties, J. Nnaomaterials 2012 (2012) 560310, https://doi.org/10.1155/2012/560310.
[43] P. Sakthivel, Pragati Kumar, M. Dhavamurthyc, Arun Thirumurugand, S. Sridhar, Structural, morphological, optical, photoluminescent and electrochemical

performance of ZnS quantum dots: influence of Mn2+ and La3+ ions, J. Mol. Struct 1288 (2023) 135723, https://doi.org/10.1016/j.molstruc.2023.135723.
[44] R. Shahid, M.S. Toprak, M. Muhammed, Microwave-assisted low temperature synthesis of wurtzite ZnS quantum dots, J. Solid. State. Chem 187 (2012) 130–133, https://doi.org/10.1016/j.jssc.2012.01.007.
[45] A.B. Lavand, M.N. Bhatu, Y.S. Malghe, Visible light photocatalytic degradation of malachite green using modified titania, J. Mater. Res. Technol. 8 (2019) 299–308, https://doi.org/10.1016/j.jmrt.2017.05.019.
[46] H.B. Ahn, J.Y. Lee, Effects of a low-temperature sulfidation process on the microstructural properties of ZnO nanowires: znS formation and nanoscale Kirkendall effect, CrystEngComm 15 (2013) 6709–6714, https://doi.org/10.1039/c3ce40403j.
[47] H. Trabelsi, P. Atheba, G.K. Gbassi, M. Ksibi, P. Drogui, Sunlight-activated photocatalysis of malachite green using a TiO2 /Cellulosic fiber, Int. J. Hazardous Mater. 1 (2012) 6–10.
[48] C.C. Chen, C.S. Lu, Y.C. Chung, J.L. Jan, UV light induced photodegradation of malachite green on TiO2 nanoparticles, J. Hazard. Mater 141 (2007) 520–528, https://doi.org/10.1016/j.jhazmat.2006.07.011.
[49] Y. Ju, S. Yang, Y. Ding, C. Sun, A. Zhang, L. Wang, Microwave-assisted rapid photocatalytic degradation of malachite green in TiO2 suspensions: mechanism and pathways, J. Phys. Chem. A 112 (2008) 11172–11177, https://doi.org/10.1021/jp804439z.
[50] J. Li, Y. Xu, Y. Liu, D. Wu, Y. Sun, Synthesis of hydrophilic ZnS nanocrystals and their application in photocatalytic degradation of dye pollutants, China Particuol. 2 (2004) 266.
[51] C.L. Torres-Martínez, R. Kho, O.I. Mian, R.K. Mehra, Efficient photocatalytic degradation of environmental pollutants with mass-produced ZnS nanocrystals, J. Colloid. Interface. Sci 240 (2001) 525, https://doi.org/10.1006/jcis.2001.7684.
[52] M.R. Hoffmann, S.T. Martin, W. Choi, D.W. Bahnemann, Environmental applications of semiconductor photocatalysis, Chem. Rev. 95 (1995) 69–96.
[53] R. Chauhan, A. Kumar, R. Chaudhary, Photocatalytic degradation of methylene blue with Fe doped ZnS nanoparticles, Spectrochimica. Acta. Part. A 113 (2013) 250–256, https://doi.org/10.1016/j.saa.2013.04.087.
[54] P. Sakthivel, S. Muthukumaran, Influence of Co2+ on electrical and optical behavior of Mn2+-doped ZnS quantum dots, Opt. Laser. Technol 103 (2018) 109–117, https://doi.org/10.1016/j.optlastec.2018.01.025.
[55] A.T. Amigun, F.A. Adekola, J.O. Tijani, S. Mustapha, Photocatalytic degradation of malachite green dye using nitrogen/sodium/iron-TiO2 nanocatalysts, Results. Chem 4 (2022), https://doi.org/10.1016/j.rechem.2022.100480.